High-Resolution Quantum Sensing Using Rydberg Atomic Receiver: Principles, Implementations, and Future Prospects

Minze Chen, Tianqi Mao, *Member, IEEE*, Zhiao Zhu, Haonan Feng, Ge Gao, Zhonghuai Wu, Wei Xiao, Zhongxiang Li, Dezhi Zheng, George K. Karagiannidis, *Fellow, IEEE*, Zhaocheng Wang, *Fellow, IEEE*, and Sheng Chen, *Life Fellow, IEEE*

***Abstract*—Quantum sensing using Rydberg atoms offers unprecedented opportunities for next-generation radar systems, transcending classical limitations in miniaturization and spectral agility. This work proposes a quantum-enhanced radar reception architecture that replaces conventional antenna-to-mixer chains with a centimeter-scale vapor cell as a quantum radio frequency (RF) field sensor and mixer, enabling this paradigm for radar sensing. This approach is based on electromagnetically induced transparency, which uses Autler-Townes splitting to enable direct RF-to-optical downconversion within the atomic medium via an external co-frequency reference. To circumvent the range-resolution limitation imposed by the narrow instantaneous response of the atomic receiver, we adopt a stepped-frequency synthesis strategy involving the hybrid manipulation of Rydberg energy states. This strategy combines coarse laser frequency tuning with fine AC-Stark shift compensation. Additionally, we establish a nonlinear response model of the Rydberg atomic homodyne receiver and propose a customized nonlinear compensation method that extends the linear dynamic range by over 7 dB. We developed a compressive sensing-based algorithm (CS-Rydberg) to suppress noise and mitigate the undersampling problem. Experimentally, we demonstrate a compact prototype that achieves centimeter-level ranging precision (RMSE = 1.06 cm) within 1.6–1.9 m. By synthesizing a 1-GHz equivalent bandwidth via sparse stepped-frequency sampling over 2.6–3.6 GHz, we observe resolvable target separations down to 15 cm under controlled sparse scenarios. These results validate the feasibility of quantum sensing based on Rydberg atomic receivers and underscore the architecture's scalability. By harnessing the atoms' ultra-broad spectral response, the synthesized bandwidth can extend well beyond the current range. This enables sub-centimeter resolution in future radar systems while preserving quantum-traceable calibration and a highly simplified front end.**

***Index Terms*—Quantum sensing, Rydberg atomic receiver, radar ranging, homodyne detection, nonlinear response.**

Received 26 July 2025; revised 16 June 2026; accepted 4 August 2026. Date of publication 27 August 2026; date of current version 14 September 2026. This work was supported in part by Beijing Outstanding Young Scientist Program under Grant JWZQ20240101014, in part by Beijing Nova Program under Grant 202604841146, in part by the National Natural Science Foundation of China under Grant 62401054 and Grant 12574312, in part by Beijing Institute of Technology Research Fund Program for High Level Talents under Grant RCPT-6120230097, in part by the State Key Laboratory of Environment Characteristics and Effects for Near-Space under Grant 2025NS10, and in part by the National Key Laboratory of Science and Technology on Space-Born Intelligent Information Processing under Grant TJ-03-24-04 and Grant TJ-01-22-06. *(Corresponding authors: Tianqi Mao; Dezhi Zheng.)*

Minze Chen, Zhiao Zhu, Ge Gao, Wei Xiao, and Dezhi Zheng are with the State Key Laboratory of Environment Characteristics and Effects for Near-Space, Beijing Institute of Technology, Beijing 100081, China, also with the MIIT Key Laboratory of Complex-Field Intelligent Exploration, Beijing Institute of Technology, Beijing 100081, China, and also with the School of Interdisciplinary Science, Beijing Institute of Technology, Beijing 100081, China (e-mail: chenmz22@bit.edu.cn; zza14606@bit.edu.cn; gao_ge@bit.edu.cn; xiao_wei@bit.edu.cn; zhengdezhi@bit.edu.cn).

Tianqi Mao is with the State Key Laboratory of Environment Characteristics and Effects for Near-Space, Beijing Institute of Technology, Beijing 100081, China, also with the MIIT Key Laboratory of Complex-Field Intelligent Exploration, Beijing Institute of Technology, Beijing 100081, China, also with the School of Interdisciplinary Science, Beijing Institute of Technology, Beijing 100081, China, and also with Beijing Institute of Technology (Zhuhai), Zhuhai 519088, China (e-mail: maotq@bit.edu.cn).

Haonan Feng and Zhongxiang Li are with the State Key Laboratory of Environment Characteristics and Effects for Near-Space, Beijing Institute of Technology, Beijing 100081, China, also with the MIIT Key Laboratory of Complex-Field Intelligent Exploration, Beijing Institute of Technology, Beijing 100081, China, also with the School of Interdisciplinary Science, Beijing Institute of Technology, Beijing 100081, China, and also with the Yangtze Delta Region Academy of Beijing Institute of Technology, Jiaxing 314019, China (e-mail: fenghn@bit.edu.cn; lizhongxiang@bit.edu.cn).

Zhonghuai Wu is with the State Key Laboratory of Environment Characteristics and Effects for Near-Space, Beijing Institute of Technology, Beijing 100081, China, also with the MIIT Key Laboratory of Complex-Field Intelligent Exploration, Beijing Institute of Technology, Beijing 100081, China, and also with the School of Interdisciplinary Science and the School of Optics and Photonics, Beijing Institute of Technology, Beijing 100081, China (e-mail: wuzhonghuai@bit.edu.cn).

George K. Karagiannidis is with the Department of Electrical and Computer Engineering, Aristotle University of Thessaloniki, 54124 Thessaloniki, Greece (e-mail: geokarag@auth.gr).

Zhaocheng Wang is with the Department of Electronic Engineering, Tsinghua University, Beijing 100084, China (e-mail: zcwang@tsinghua.edu.cn).

Sheng Chen is with the School of Electronics and Computer Science, University of Southampton, SO17 1BJ Southampton, U.K., and also with the Faculty of Information Science and Technology, Ocean University of China, Qingdao 266100, China (e-mail: sqc@ecs.soton.ac.uk).

Digital Object Identifier 10.1109/JSAC.2026.3727957
Digital Object Identifier 10.1109/JSAC.2026.3727957

I. Introduction

By USING quantum coherence to overcome classical detection constraints, quantum sensing has revolutionized precision measurement [1], [2]. This method allows microwave electrometry with remarkable sensitivity and spectral coverage when used for electromagnetic field detection, which is crucial for next-generation radar systems [3], [4]. However, there are inherent trade-offs between bandwidth, sensitivity, and miniaturisation in conventional radar systems. Multiple distinct receiver front-ends and processing modules for distinct bands are required for frequency agility, which greatly increases system complexity. Large-aperture antennas are necessary for high-sensitivity reception while still being limited by the thermal noise floor [5]. For ranging applications, which are essential to contemporary remote sensing and Earth observation, these restrictions become severely restrictive. The main explanation is that the system bandwidth determines

TABLE I
COMPARISON OF CLASSICAL MICROWAVE RECEIVER AND RYDBERG ATOMIC RECEIVER

Feature	Classical Receiver	Atomic Receiver
Bandwidth	Tunable bandwidth: $\sim$10 GHz [17]	Tunable bandwidth: DC – THz
	Instantaneous bandwidth: $\sim$1 GHz [17]	Instantaneous bandwidth: $<$ 10 MHz
Sensitivity Limit	Thermal Noise Limited	Quantum Noise Limited
Size	Wavelength-dependent	mm-cm Vapor Cell [18]
Calibration	Requires External Reference	Self-Calibrated
Architecture	Antenna + LNA + Mixer + filter	Atomic RF Sensor/Mixer + Optical Readout

the achievable range resolution. Additionally, there are strict requirements for integration density and sensitivity when deploying on platforms with limited space and load, such as satellites [6]. Therefore, it is essential to investigate new radar reception designs that can get around these basic limitations [7].

Rydberg atomic microwave electrometry, an innovative advancement in quantum sensing, establishes a novel framework for electromagnetic field detection [8]. Rydberg atomic sensors employ alkali metal atoms (such as caesium or rubidium) that are driven to highly sensitive Rydberg states using coherent laser stimulation. These sensors have been experimentally demonstrated to possess sensitivities about equal to $\mathrm{nV \cdot cm^{-1} \cdot Hz^{-1/2}}$ [9], [10]. Theoretically, there exists at least one further order of magnitude of expansion potential to surpass the thermal noise threshold of traditional receivers. The response frequency range can be adjusted from DC to terahertz without the need for component replacement. Rydberg atom sensing can be self-calibrated by the inherent characteristics of the atoms. Simultaneously, it can be compactly incorporated within a vapor cell of less than one centimetre. Furthermore, in contrast to high-frequency classical antennas that intrinsically demonstrate significant directionality, Rydberg-based sensors possess a virtually omnidirectional response throughout the whole electromagnetic spectrum [11]. A comparison between the classical microwave receiver and the Rydberg atomic receiver is summarized in Table I. The fundamental detecting method, utilising electromagnetically induced transparency (EIT) and Autler-Townes (AT) splitting, facilitates concurrent radio frequency (RF)-to-optical conversion and coherent mixing, devoid of the conventional electronic noise and distortion associated with standard receivers. It facilitates integrated measurement capabilities for intensity quantification [8], precise frequency discrimination [12], polarisation analysis [13], [14], and phase-sensitive detection [9], [15], [16], all within a cohesive, coherent physical framework. The Rydberg atomic sensor has garnered considerable interest as a pivotal device poised to transform traditional microwave electrometry regarding sensitivity, dimensions, and spectrum agility.

Advancements in remote sensing utilising Rydberg atomic receivers are underway. Experimental validations thus far have shown atomic sensing capabilities for detecting moving targets [19], determining angle of arrival [20], positioning with multiple base stations [21], implementing digital beamforming [22], and facilitating communication amidst dynamic radar interference [23]. However, substantial challenges remain in their practical application for radar ranging tasks. The reception frequency of Rydberg atoms can be continuously adjusted across the entire band. However, the intrinsic response bandwidth within a single EIT window is generally less than 10 MHz, constrained by the atomic lifetime limitations [24], [25]. No studies have reported methods anticipated to overcome this limitation. The theoretical radar resolution is constrained to approximately 15 meters, which does not satisfy the fundamental requirements for applications [26]. Studies have investigated continuous frequency detection capabilities in the presence of external electromagnetic fields [27], [28]. However, existing methodologies exhibit significant sensitivity deterioration at frequencies deviating from atomic resonance. A recent study introduced a theoretical framework for Rydberg atomic radar ranging utilising linear frequency modulation (LFM) signals [29]. Nonetheless, the chirp bandwidth employed remains confined to a narrow EIT response window, which does not satisfy the resolution and sensitivity demands of practical radar applications. The engineering feasibility of the study requires further demonstration. To our knowledge, there has been no reported comprehensive experimental verification of Rydberg-based radar ranging. The architectural design, engineering implementation, response modelling, and data processing algorithms of the Rydberg atomic radar represent significant research gaps.

This paper presents a new radar architecture that combines Rydberg atomic homodyne detection with a stepped-frequency waveform strategy, utilising quantum sensitivity benefits and addressing the inherent resolution limitations. This study presents a calibration and ranging algorithm framework that addresses the challenges posed by the unique characteristics of atomic receivers, including atomic nonlinear responses, spatial local oscillator (LO) multipath effects, and system sensitivity in practical implementations. This study's main contributions are summarised below.

- We develop a novel radar sensing framework based on a Rydberg atomic receiver. By leveraging laser frequency tuning and AC-Stark-effect-based fine adjustment, the atomic reception mechanism enables the detection of stepped frequency continuous waveform (SFCW) signals, facilitating synthesized wideband sensing from discrete frequency points. This framework is inherently scalable to higher bandwidths and increased frequency-domain sampling density.
- We establish an analytical nonlinear response model for Rydberg atomic homodyne receivers. Building on the model, we propose a dedicated nonlinear compensation technique to achieve rapid phase correction, improving linear dynamic range by over 7 dB.
- Addressing sensitivity challenges unique to Rydberg atomic radar, we introduce a dedicated compressive-sensing-based algorithm framework, called CS-Rydberg.
- To the best of our knowledge, we are the first to implement a compact ranging system based on a Rydberg

atomic receiver. Experimental results demonstrate centimeter-level ranging precision (RMSE = 1.06 cm) in the range of 1.6-1.9 m, with an observable resolution down to 15 cm for sparse targets under controlled conditions.

II. System Model

A. Stepped-Frequency Signal Model

High-resolution ranging requires a large effective RF bandwidth. In contrast to conventional receivers, the Rydberg-atomic receiver provides ultra-sensitive field-to-optical transduction but exhibits an intrinsically narrow instantaneous response centered around an atomic transition. This unique "narrowband-yet-tunable" characteristic motivates a frequency-synthesis strategy rather than a physical broadening of the atomic response. Specifically, the SFCW strategy does not extend the instantaneous EIT–AT bandwidth. Instead, the receiver remains narrowband at each dwell and is tuned near resonance with the current single-tone carrier. The equivalent wideband response is obtained by coherently accumulating the complex measurements over multiple stepped frequencies, so that the target-delay information is reconstructed from the frequency-dependent phase evolution across the synthesized frequency aperture. To synthesize a wide effective bandwidth while confining the atomic receiver to its narrow instantaneous response window, we adopt a SFCW waveform in which the transmitter radiates a sequence of single-tone carriers. Over one sweep, the transmitted signal is expressed as

$$s(t) = \sum_{k=1}^{K} E_{\mathrm{SIG}}^{0} \cdot \mathrm{rect}\left(\frac{t - t_k - T_k/2}{T_k}\right) \times \exp[\mathrm{j}\left(2\pi f_k t + \phi_k\right)], \tag{1}$$

where t is time, K is the number of frequency points in one sweep, f_k is the k-th carrier frequency, T_k is the dwell time spent at f_k, and $t_k = \sum_{i=1}^{k-1} T_i$ denotes the start time of the k-th dwell. The function $\mathrm{rect}(x)$ equals 1 for $|x| \leq 0.5$ and 0 otherwise, ensuring that only the k-th tone is active during its dwell. The constant E_{SIG}^{0} denotes the transmitted field amplitude referenced to the receiver plane before propagation losses are applied, and ϕ_k is the initial phase of the k-th tone at the transmitter. Importantly, we do not require $\{f_k\}_{k=1}^{K}$ to be uniformly spaced. In our system, the available reception frequencies are constrained by quantum-state-selective atomic resonances and fine tuning, so the stepped grid is naturally non-uniform.

After propagation and reflection from the scene, the RF field arriving at the vapor cell is the superposition of echoes from M paths, modeled as

$$E_{\mathrm{RX}}(t) = \sum_{k=1}^{K} \sum_{m=1}^{M} \eta_m E_{\mathrm{SIG}}^{0} \,\mathrm{rect}\left(\frac{t - \tau_m - t_k - T_k/2}{T_k}\right) \times \exp[\mathrm{j}\left(2\pi f_k (t - \tau_m) + \phi_k\right)], \tag{2}$$

where η_m is the complex attenuation of the m-th path such as capturing path loss, reflection coefficient, and any fixed phase offset not explicitly modeled elsewhere, and τ_m is the corresponding two-way delay. For a specular reflection from a target at range R_m, the delay is $\tau_m \approx 2R_m/c$, where c is the speed of light. The form $\exp[-\mathrm{j}2\pi f_k \tau_m]$ makes explicit that the range information is encoded as a frequency-dependent phase rotation. This is precisely why the SFCW paradigm is used for ranging.

To enable coherent phase-sensitive reception at each stepped frequency without relying on a wideband electronic mixer chain, a co-frequency LO field is radiated toward the vapor cell as a phase reference. The LO field at the cell is modeled as

$$E_{\mathrm{LO}}(t) = \sum_{k=1}^{K} E_{\mathrm{LO}}^{0} \cdot \mathrm{rect}\left(\frac{t - \tau_{\mathrm{LO}} - t_k - T_k/2}{T_k}\right) \times \exp[\mathrm{j}\left(2\pi f_k (t - \tau_{\mathrm{LO}}) + \phi_{\mathrm{LO},k}\right)], \tag{3}$$

where E_{LO}^{0} is the LO field amplitude at the cell, $\tau_{\mathrm{LO}} = D/c$ is the (one-way) propagation delay from the LO horn to the cell with fixed distance D, and $\phi_{\mathrm{LO},k}$ is the initial phase of the LO at the k-th tone. The LO path is designed to be short and stable so that τ_{LO} is constant and calibratable. In practice, the echo and LO tones are generated from the same RF synthesizer, so their relative phase is stable within each dwell ($\phi_{\mathrm{LO},k} \approx \phi_k$). The total RF field that drives the atomic sensor is therefore $E_{\mathrm{tot}}(t) = E_{\mathrm{RX}}(t) + E_{\mathrm{LO}}(t)$, and the subsequent receiver model will map this composite field into an optical-domain observable for ranging.

B. Rydberg Atomic Receiving Model

The receiver front-end is a four-level ladder-type Cs-133 system that converts an incident RF electric field into an optical-domain observable through EIT and AT splitting. As shown in Fig. 1(a), a weak probe laser at 852 nm couples the ground state $|1\rangle = 6S_{1/2}$ to the intermediate state $|2\rangle = 6P_{3/2}$ with Rabi frequency Ω_{p}, while a strong coupling laser at 509 nm drives $|2\rangle \to |3\rangle = nD_{5/2}$ with Rabi frequency Ω_{c}. This optical ladder establishes an EIT window in the probe transmission, which provides a narrow and highly sensitive transduction channel. The incident RF field couples the Rydberg state $|3\rangle$ to a nearby state $|4\rangle$ with an RF Rabi frequency Ω_{RF}, producing AT splitting whose magnitude depends on the RF field strength.

The quantum dynamics of the driven and dissipative four-level system are described by the Lindblad master equation formulated as

$$\dot{\rho} = -\frac{\mathrm{j}}{\hbar}[H, \rho] + \sum_q \gamma_q \left(L_q \rho L_q^{\dagger} - \frac{1}{2}\{L_q^{\dagger} L_q, \rho\}\right), \tag{4}$$

where ρ is the 4×4 density matrix, j is the imaginary unit, $\hbar$ is the reduced Planck constant, and $[H, \rho] = H\rho - \rho H$ denotes the commutator. The operators L_q represent dissipative channels and γ_q are the corresponding rates, which include spontaneous decay on the optical transition $|2\rangle \to |1\rangle$ with rate γ_{21} and effective decoherence of the Rydberg manifold summarized by γ_3. Under the rotating-wave approximation

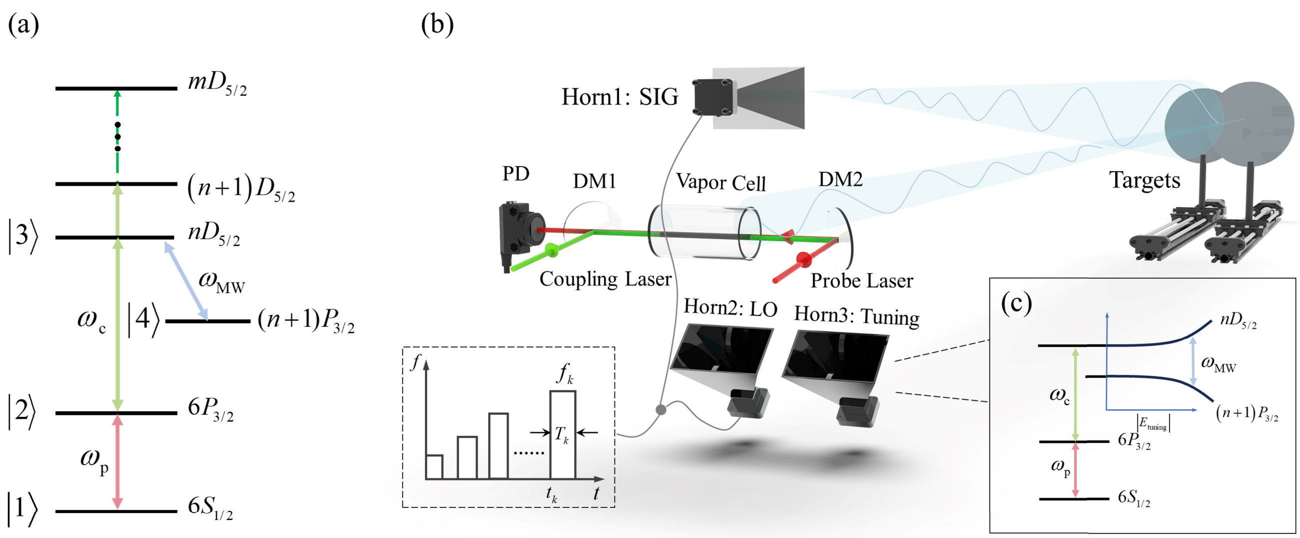

Fig. 1. Energy-level diagrams and ranging methods of the proposed system (DM: dichroic mirror. PD: photodetector). (a) A four-level structure enables single-frequency signal reception via EIT and AT splitting. Multi-frequency reception is achieved by switching Rydberg states through laser frequency tuning. (b) The frequency hopping of the signal is synchronized with the laser frequency tuning, ensuring that both the echo signal and the LO field are resonantly received and coherently downconverted to a DC optical readout. (c) Continuous frequency tunability is realized using an additional far-detuned field.

(RWA), the bare Hamiltonian without the far-detuned tuning field is written as

$$H^{(0)} = \frac{\hbar}{2}\begin{bmatrix} 0 & \Omega_{\mathrm{p}} & 0 & 0 \\ \Omega_{\mathrm{p}}^{*} & -2\Delta_{\mathrm{p}} & \Omega_{\mathrm{c}} & 0 \\ 0 & \Omega_{\mathrm{c}}^{*} & -2(\Delta_{\mathrm{p}}+\Delta_{\mathrm{c}}) & \Omega_{\mathrm{RF}} \\ 0 & 0 & \Omega_{\mathrm{RF}}^{*} & -2(\Delta_{\mathrm{p}}+\Delta_{\mathrm{c}}+\Delta_{\mathrm{RF}}^{(0)}) \end{bmatrix}, \tag{5}$$

where Ω_{p} and Ω_{c} are the probe and coupling Rabi frequencies, Ω_{RF} is the RF Rabi frequency on the $|3\rangle \leftrightarrow |4\rangle$ transition, and Δ_{p}, Δ_{c}, and $\Delta_{\mathrm{RF}}^{(0)}$ are the corresponding detunings from the bare transitions. When the far-detuned tuning field is applied during the k-th dwell, it does not enter the off-diagonal RF coupling term as an additional resonant signal. Instead, after eliminating its rapidly oscillating component, its leading-order contribution is a diagonal AC-Stark shift of the Rydberg states. The effective Hamiltonian used at the k-th dwell is therefore

$$H_k = H^{(0)} + \hbar\,\mathrm{diag}\,(0, 0, \delta_{3,k}, \delta_{4,k})\,, \tag{6}$$

where $\delta_{3,k}$ and $\delta_{4,k}$ are the AC-Stark-induced angular-frequency shifts of states $|3\rangle$ and $|4\rangle$, respectively. For a far-detuned tuning field, they can be approximated as

$$\delta_{i,k} = \frac{\alpha_i(\omega_{\mathrm{tuning}})}{4\hbar}\,|E_{\mathrm{tuning},k}|^2\,, \quad i = 3, 4, \tag{7}$$

where $\alpha_i(\omega_{\mathrm{tuning}})$ is the dynamic polarizability of state $|i\rangle$ at the tuning-field angular frequency ω_{tuning}, and $E_{\mathrm{tuning},k}$ is the tuning-field amplitude at the k-th dwell. In the experiments, the probe and coupling lasers are frequency-stabilized and operated near two-photon resonance so that $\Delta_{\mathrm{p}} \approx 0$ and $\Delta_{\mathrm{c}} \approx 0$ at the selected Rydberg state, which maximizes the EIT contrast and yields a well-defined operating point.

The RF drive entering (5) is produced by the total incident RF field at the cell, $E_{\mathrm{tot}}(t) = E_{\mathrm{RX}}(t) + E_{\mathrm{LO}}(t)$ defined in Section II-A. Since (5) is formulated under the RWA, the RF coupling term is determined by the slowly varying complex envelope rather than the fast carrier oscillation. Assuming the dwell time T_k is sufficiently long compared to the propagation delays ($T_k \gg \tau_m, \tau_{\mathrm{LO}}$), the envelopes of the LO and echo signals overlap substantially. Thus, during the effective dwell interval, the near-resonant total RF field at the cell can be approximated as

$$\begin{aligned} E_{\mathrm{tot}}(t) &\approx \sum_{k=1}^{K} \tilde{E}_{\mathrm{tot},k}\,\mathrm{rect}\left(\frac{t - t_k - T_k/2}{T_k}\right)\exp(\mathrm{j}2\pi f_k t)\,, \\ \tilde{E}_{\mathrm{tot},k} &= \tilde{E}_{\mathrm{LO},k} + \tilde{E}_{\mathrm{RX},k}, \end{aligned} \tag{8}$$

where $\tilde{E}_{\mathrm{tot},k}$ is the complex envelope that captures the coherent superposition between the LO and the echo at the stepped carrier f_k. Using (2)–(3), one may equivalently write

$$\begin{aligned} \tilde{E}_{\mathrm{RX},k} &= \sum_{m=1}^{M} \eta_m E_{\mathrm{SIG}}^{0} \exp[\mathrm{j}\,(\phi_k - 2\pi f_k \tau_m)]\,, \\ \tilde{E}_{\mathrm{LO},k} &= E_{\mathrm{LO}}^{0} \exp[\mathrm{j}\,(\phi_{\mathrm{LO},k} - 2\pi f_k \tau_{\mathrm{LO}})]\,. \end{aligned} \tag{9}$$

Accordingly, in the RWA Hamiltonian (5), the RF Rabi frequency is determined by this envelope and is effectively constant within each dwell denoted as

$$\begin{aligned} \Omega_{\mathrm{RF}}(t) &= \sum_{k=1}^{K} \Omega_{\mathrm{RF},k}\,\mathrm{rect}\left(\frac{t - t_k - T_k/2}{T_k}\right), \\ \Omega_{\mathrm{RF},k} &= \frac{d_{34}}{\hbar}\,\tilde{E}_{\mathrm{tot},k}, \end{aligned} \tag{10}$$

where d_{34} is the effective electric dipole matrix element between $|3\rangle$ and $|4\rangle$.

As described in (6) and (7), its leading-order effect in the far-detuned regime is to produce diagonal Stark shifts of the Rydberg states. The relevant quantity for RF reception is the differential Stark shift between $|3\rangle$ and $|4\rangle$, which changes the effective transition frequency. Specifically, the $|3\rangle \leftrightarrow |4\rangle$ transition frequency is formulated as

$$\begin{aligned} f_{34,k} &= f_{34}^{(0)} + \Delta f_{34,k}, \\ \Delta f_{34,k} &= \frac{\delta_{4,k} - \delta_{3,k}}{2\pi} = \frac{\alpha_{\mathrm{AC}}}{4h} \left| E_{\mathrm{tuning},k} \right|^2, \end{aligned} \tag{11}$$

where $f_{34}^{(0)}$ is the unperturbed transition frequency, α_{AC} is the differential AC polarizability relevant to the $|3\rangle$ and $|4\rangle$ pair, and h is Planck's constant. For the k-th stepped tone at frequency f_k, the RF detuning in (5) is expressed as

$$\begin{aligned} \Delta_{\mathrm{RF},k} &= 2\pi(f_k - f_{34}) \\ &= 2\pi\left(f_k - f_{34}^{(0)} - \Delta f_{34}\right), \end{aligned} \tag{12}$$

and is piecewise constant over the sweep written as

$$\Delta_{\mathrm{RF}}(t) = \sum_{k=1}^{K} \Delta_{\mathrm{RF},k} \operatorname{rect}\left(\frac{t - t_k - T_k/2}{T_k}\right). \tag{13}$$

In operation, the tuning-field amplitude is synchronised with the SFCW dwell such that $f_{34}(E_{\mathrm{tuning},k}) \approx f_k$, ensuring the atomic transition stays resonant with the instantaneous stepped carrier. Therefore, $\Delta_{\mathrm{RF},k}$ captures only the residual detuning error, while the range-dependent phase is encoded by the propagation term $\exp(-\mathrm{j}2\pi f_k \tau_m)$ in (2), which is the basis of the SFCW ranging reconstruction. By treating AC-Stark tuning as a detuning control, the receiver response can be described within a single unified quantum framework.

The optical readout is obtained from the probe coherence ρ_{21}, because the induced polarization on the probe transition is proportional to ρ_{21} and directly determines probe absorption and dispersion. Under the weak-probe approximation, the electric susceptibility at the probe frequency can be expressed in the standard form modeled as

$$\chi(t) = \frac{N|d_{21}|^2}{\epsilon_0 \hbar} \frac{\rho_{21}(t)}{\Omega_{\mathrm{p}}}, \tag{14}$$

where N is the atomic number density, d_{21} is the dipole matrix element of the $|1\rangle \leftrightarrow |2\rangle$ transition, and ϵ_0 is the vacuum permittivity. The probe transmission through a vapor cell of length L is then described by Beer–Lambert propagation, and the normalized transmitted probe power can be written as

$$T_{\mathrm{probe}}(t) \triangleq \frac{P_{\mathrm{out}}(t)}{P_{\mathrm{in}}(t)} = \exp\left[-k_{\mathrm{p}} L \operatorname{Im}\left(\chi(t)\right)\right], \tag{15}$$

where $P_{\mathrm{in}}(t)$ and $P_{\mathrm{out}}(t)$ are the incident and transmitted probe powers, $k_{\mathrm{p}} = 2\pi/\lambda_{\mathrm{p}}$ is the probe wavenumber with probe wavelength $\lambda_{\mathrm{p}} = 852\,\mathrm{nm}$, and $\operatorname{Im}(\chi)$ is proportional to $\operatorname{Im}(\rho_{21})$. The photodetector converts the transmitted optical power into an electrical signal formulated as

$$i_{\mathrm{PD}}(t) = \mathcal{R}_{\mathrm{PD}}\, P_{\mathrm{out}}(t) + i_n(t), \tag{16}$$

where $\mathcal{R}_{\mathrm{PD}}$ is the photodetector responsivity and $i_n(t)$ represents the aggregate detection noise, including shot noise and technical noise. In the proposed system, the stepped-frequency RF excitation is synchronized with laser tuning and AC-Stark control such that, within each dwell interval, the parameters in (4)–(16) can be treated as quasi-static. Consequently, one can associate each frequency point f_k with a corresponding time-averaged detector output sample extracted from $i_{\mathrm{PD}}(t)$, which serves as the input observable for subsequent coherent ranging reconstruction.

III. Proposed Rydberg Atomic Ranging Scheme

A. High-Resolution Rydberg Atomic Sensing

The frequency agility of Rydberg atomic homodyne receiver originates from quantum state-selective RF reception governed by EIT windows. However, the intrinsic narrow instantaneous bandwidth of Rydberg transitions severely limits ranging applications, as the range resolution fundamentally depends on the transmitted signal bandwidth given by

$$\Delta r = \frac{c}{2B}, \tag{17}$$

where c is the speed of light and B represents the effective bandwidth. This necessitates a frequency-hopping scheme across multiple Rydberg transitions to synthesize GHz-level bandwidth, enabling narrowband reception while achieving broadband-equivalent resolution.

For each frequency point, the transmitter radiates a single-tone carrier during a dwell interval of duration T_k as modeled in (1). Meanwhile, the atomic receiver is configured such that its effective reception frequency matches the transmitted tone by selecting the Rydberg transition and applying AC-Stark tuning. Specifically, for the k-th dwell, the tuned transition frequency is $f_{\mathrm{RX},k} = f_{34}^{(0)} + \Delta f_{34,k}$ with $\Delta f_{34,k}$ controlled by the far-detuned field E_{tuning}, and the RF detuning in (5) becomes $\Delta_{\mathrm{RF},k} = 2\pi(f_k - f_{\mathrm{RX},k})$. This design ensures that $\Delta_{\mathrm{RF},k}$ can be kept close to zero at each point, so that the receiver operates near a well-defined, high-sensitivity working point while the overall sweep spans a wide effective bandwidth that determines the achievable range resolution.

At the vapor cell, the incident RF field is the coherent sum of the echo field $E_{\mathrm{RX}}(t)$ and the local-oscillator field $E_{\mathrm{LO}}(t)$ defined in (2) and (3), yielding $E_{\mathrm{tot}}(t) = E_{\mathrm{RX}}(t) + E_{\mathrm{LO}}(t)$. Through (10), this composite field drives the Rydberg transition with RF Rabi frequency $\Omega_{\mathrm{RF}}(t) = (d_{34}/\hbar)E_{\mathrm{tot}}(t)$. The quantum dynamics governed by (4)–(5) determine the probe coherence $\rho_{21}(t)$, which sets the optical susceptibility $\chi(t)$ via (14) and thus the transmitted probe power through (15). The photodetector converts the transmitted probe power into an electrical current $i_{\mathrm{PD}}(t)$. Within each dwell, the system is operated in a quasi-static regime in which the laser parameters, the tuning field, and the scene-induced delays can be treated as constant over T_k, so the receiver output can be summarized by a single sample extracted from $i_{\mathrm{PD}}(t)$ by time averaging or synchronous demodulation over the dwell interval.

To recover phase information required for ranging, quadrature homodyne reception is implemented by using two LO phase biases separated by 90° at the same carrier frequency f_k. During the k-th dwell, define the complex RF Rabi envelopes at the vapor cell as $\Omega_{\mathrm{LO},k} \triangleq (d_{34}/\hbar)\tilde{E}_{\mathrm{LO},k}$ and $\Omega_{\mathrm{RX},k} \triangleq (d_{34}/\hbar)\tilde{E}_{\mathrm{RX},k}$. Applying an LO phase bias φ amounts to $\Omega_{\mathrm{LO},k} \to \Omega_{\mathrm{LO},k} e^{\mathrm{j}\varphi}$, and the composite drive magnitude that enters the quasi-static atomic transduction can be written as

$$\Omega_{\mathrm{tot},k}^{(\varphi)} \triangleq \left| \Omega_{\mathrm{LO},k} e^{\mathrm{j}\varphi} + \Omega_{\mathrm{RX},k} \right|. \tag{18}$$

After averaging over T_k, the photodetector output at that bias can be summarized as a nonlinear mapping of this magnitude formulated as

$$\bar{z}_k^{(\varphi)} \approx \mathcal{S}_k\left(\Omega_{\mathrm{tot},k}^{(\varphi)}; \Delta_{\mathrm{RF},k}\right) + n_k^{(\varphi)}, \tag{19}$$

where $\mathcal{S}_k(\cdot)$ is the effective RF-to-optical transduction induced by the atomic medium under the operating configuration of the k-th point. Because AC-Stark control actively maintains $\Delta_{\mathrm{RF},k} \approx 0$ and the optical readout is an intensity measurement, the dominant dependence near the working region is on the magnitude $\Omega_{\mathrm{tot},k}^{(\varphi)}$.

Writing $\Omega_{\mathrm{RX},k} = A_k e^{\mathrm{j}\theta_k}$ with $A_k \geq 0$ and θ_k being the LO-referenced echo phase, and assuming the echo is weak relative to the LO, $A_k \ll |\Omega_{\mathrm{LO},k}|$, the magnitude in (18) admits a first-order expansion expressed as

$$\Omega_{\mathrm{tot},k}^{(\varphi)} \approx |\Omega_{\mathrm{LO},k}| + A_k \cos(\theta_k - \varphi). \tag{20}$$

Linearizing the nonlinear mapping in (19) around the LO bias point is written by

$$\begin{aligned} \bar{z}_k^{(\varphi)} &\approx \mathcal{S}_k(|\Omega_{\mathrm{LO},k}|; 0) + \kappa_k\, A_k \cos(\theta_k - \varphi) + n_k^{(\varphi)}, \\ \kappa_k &\triangleq \left.\frac{\partial \mathcal{S}_k(\Omega; 0)}{\partial \Omega}\right|_{\Omega = |\Omega_{\mathrm{LO},k}|}. \end{aligned} \tag{21}$$

A reference measurement with the echo path blocked removes the constant background term $\mathcal{S}_k(|\Omega_{\mathrm{LO},k}|; 0)$, yielding observables $\Delta z_k^{(\varphi)} = \bar{z}_k^{(\varphi)} - \bar{z}_{\mathrm{LO},k}^{(\varphi)}$ that satisfy

$$\Delta z_k^{(\varphi)} \approx \kappa_k\, A_k \cos(\theta_k - \varphi) + \tilde{n}_k^{(\varphi)}. \tag{22}$$

Choosing $\varphi = 0$ and $\varphi = \pi/2$ therefore produces the canonical quadratures proportional to $\cos\theta_k$ and $\sin\theta_k$, which is denoted as

$$I_k = \kappa_k\, A_k \cos(\theta_k) + n_{I,k}, \tag{23}$$

$$Q_k = \kappa_k\, A_k \sin(\theta_k) + n_{Q,k}. \tag{24}$$

Here A_k collects the echo-induced RF coupling magnitude at f_k, which includes the reflection coefficient, propagation loss, and any frequency-dependent path effects. κ_k is the local small-signal responsivity determined by the operating point of the atomic transduction. When A_k is not small compared to $|\Omega_{\mathrm{LO},k}|$, or when $\mathcal{S}_k(\cdot)$ is not locally linear over the induced perturbation range, higher-order terms neglected in (20) and in the Taylor expansion of $\mathcal{S}_k(\cdot)$ lead to gain compression and distortion, which motivates the nonlinear compensation developed in Section III-B.

The additive noise terms $n_{I,k}$ and $n_{Q,k}$ collect all fluctuations in the extracted in-phase and quadrature channels, including fundamental quantum noise and technical noise introduced by the practical readout chain. In the present room-temperature vapor-cell implementation, the measured baseband readout is in a technical-noise-limited regime. The dominant contributions arise from laser intensity and frequency noise transferred through the optical transduction, residual amplitude modulation in the optical readout, electronic noise in the photodetector and acquisition chain, and environmental RF interference [30]. These effects are broadband and can exceed the expected quantum-noise floor under the current operating conditions [9].

For completeness, we include a lower-bound estimate of the photodetector shot-noise floor. For a detected probe power P_{PD} and photodetector responsivity $\mathcal{R}_{\mathrm{PD}}$, the shot-noise-limited current spectral density is written by

$$i_{\mathrm{SN}} = \sqrt{2q\,\mathcal{R}_{\mathrm{PD}} P_{\mathrm{PD}}}\,, \tag{25}$$

where q is the electron charge.

In (23) and (24), the phase θ_k represents the relative propagation phase between the echo and the LO References at frequency f_k. For a single dominant reflection at range R with two-way delay $\tau = 2R/c$, and an LO reference path of length D with delay $\tau_{\mathrm{LO}} = D/c$, the phase is expressed as

$$\theta_k = -2\pi f_k \tau + 2\pi f_k \tau_{\mathrm{LO}} + \Delta\phi + \phi_{\mathrm{sys}}(f_k), \tag{26}$$

where $\Delta\phi$ is the initial phase offset between the transmitted/echo branch and the LO branch, and $\phi_{\mathrm{sys}}(f_k)$ represents any residual frequency-dependent phase contributed by the experimental system, including cable delays, antenna phase centers, and atomic readout latency, that is stable across sweeps and can be calibrated. Writing $\lambda_k = c/f_k$, (26) is equivalent to $\theta_k = -4\pi R/\lambda_k + 2\pi D/\lambda_k + \Delta\phi + \phi_{\mathrm{sys}}(f_k)$, consistent with a two-way ranging phase term plus a one-way LO reference term.

Combining (23)–(24) yields a complex measurement at each stepped frequency written by

$$y_k \triangleq I_k + \mathrm{j}Q_k \approx \kappa_k A_k e^{\mathrm{j}\theta_k} + w_k, \tag{27}$$

where $w_k = n_{I,k} + \mathrm{j}n_{Q,k}$. Since the LO reference delay τ_{LO} is fixed and known, it is convenient to remove this deterministic phase by defining $\tilde{y}_k = y_k \exp[-\mathrm{j}2\pi f_k \tau_{\mathrm{LO}}]$, which leads to

$$\begin{aligned} \tilde{y}_k \approx\ & \kappa_k A_k \exp\left[-\mathrm{j}\frac{4\pi f_k}{c} R\right] \\ & \times \exp[\mathrm{j}(\Delta\phi + \phi_{\mathrm{sys}}(f_k))] + \tilde{w}_k. \end{aligned} \tag{28}$$

For general scenes with M paths at ranges $\{R_m\}_{m=1}^{M}$, (28) extends to a superposition model formulated as

$$\tilde{y}_k \approx \sum_{m=1}^{M} b_{m,k} \exp\left[-\mathrm{j}\frac{4\pi f_k}{c} R_m\right] + \tilde{w}_k, \tag{29}$$

where $b_{m,k}$ absorbs the path-dependent complex amplitude and any slowly varying system phase term. Equations (28)–(29) show that ranging reduces to estimating delays/ranges from the frequency-dependent phase rotation of $\tilde{y}_k$ across the stepped grid $\{f_k\}$, while κ_k and A_k primarily modulate the amplitude. This separation motivates the subsequent nonlinear compensation that stabilizes κ_k across states and tuning conditions, and it also motivates phase-focused ranging reconstruction methods that are robust to amplitude fluctuations.

Given $\{\tilde{y}_k\}_{k=1}^{K}$, a continuous matched-filter range profile can be formed as

$$p(r) = \left|\sum_{k=1}^{K} \tilde{y}_k \exp\left(\mathrm{j}\frac{4\pi f_k}{c} r\right)\right|, \tag{30}$$

which reduces to an inverse discrete Fourier transform when $\{f_k\}$ are uniformly spaced. The achievable range resolution is primarily set by the effective swept bandwidth

$B = f_{\max} - f_{\min}$ through $\Delta r \approx c/(2B)$, while the detailed sidelobe structure depends on the specific frequency placement and the weighting implicit in $\kappa_k A_k$. For algorithmic implementation, we discretize the range axis into a grid $\mathbf{r} = [r_1, \ldots, r_{N_r}]^T$ and define the complex measurement vector $\mathbf{y} = [\tilde{y}_1, \ldots, \tilde{y}_K]^T$. The one-dimensional ranging model can then be expressed as

$$\mathbf{y} = \mathbf{\Phi}\mathbf{x} + \mathbf{w}, \qquad \mathbf{\Phi}(k, n) = \exp\left(-\mathrm{j}\frac{4\pi f_k}{c} r_n\right), \tag{31}$$

where $\mathbf{x} \in \mathbb{C}^{N_r}$ represents the complex range reflectivity profile on the grid and $\mathbf{w}$ is the noise vector. This linear model, together with the physics-informed calibration of κ_k and the non-uniform stepped grid induced by quantum-state selection and AC-Stark tuning, forms the basis for the nonlinear compensation and the one-dimensional ranging algorithm developed in the subsequent sections. To make this calibration and stabilization practical over the synthesized band, the next subsection derives a simple physically grounded local model of the atomic transduction around the operating point and uses it to construct an efficient inverse mapping for compensation.

B. Nonlinearity Compensation

The ranging model in Section III-A is built on the fact that, at each stepped frequency point f_k, the Rydberg atomic receiver provides phase-sensitive I/Q samples whose phase encodes the delay (range) through θ_k in (23)–(24). This model implicitly assumes that the receiver responsivity κ_k is well-defined and that the extracted I/Q samples are proportional to the LO–echo interference term. In a Rydberg atomic homodyne receiver, however, the mixing and downconversion do not occur in an electronic multiplier but are generated by the atomic medium itself, so the photodetected output is a nonlinear function of the composite RF Rabi frequency $\Omega_{\text{tot}} \propto |E_{\text{LO}} + E_{\text{RX}}|$ as governed by the master equation (4). Consequently, the measured time-averaged detector outputs at each dwell, denoted generically as $\bar{I}_k$ and $\bar{Q}_k$ before compensation, are more accurately described by a nonlinear mapping written as

$$\begin{aligned}\bar{I}_k &\approx \mathcal{S}_k\left(\Omega_{\text{tot},k}^{(0^\circ)}; \Delta_{\text{RF},k}\right) + n_{I,k}, \\ \bar{Q}_k &\approx \mathcal{S}_k\left(\Omega_{\text{tot},k}^{(90^\circ)}; \Delta_{\text{RF},k}\right) + n_{Q,k},\end{aligned} \tag{32}$$

where $\mathcal{S}_k(\cdot)$ represents the quasi-static RF-to-optical transduction at the k-th operating point, which includes the selected Rydberg state, laser parameters, and Doppler-broadened thermal effects. $\Delta_{\text{RF},k}$ is the effective RF detuning that already includes the AC-Stark tuned reception frequency, and $n_{I,k}, n_{Q,k}$ denote the post-detection noise terms. The composite amplitudes $\Omega_{\text{tot},k}^{(0^\circ)}$ and $\Omega_{\text{tot},k}^{(90^\circ)}$ correspond to the two LO phase biases used to form quadratures. When the echo is sufficiently weak relative to the LO, one may linearize $\mathcal{S}_k(\cdot)$ around the LO working point, and the slope of this mapping becomes the effective responsivity κ_k that appears in (23)–(24).

To support an analytically invertible effective model for $\mathcal{S}_k(\cdot)$, we specialize the master-equation transduction to the weak-probe, steady-state, near-resonant regime targeted at each step ($\Delta_{\text{p}} = \Delta_{\text{c}} = 0$ and $\Delta_{\text{RF},k} \approx 0$). In this limit, the probe coherence ρ_{21} is linear in Ω_{p} and is obtained by solving a set of linear steady-state equations for the relevant coherences, where the RF coupling enters only through the composite drive magnitude $\Omega_{\text{tot}} \propto |E_{\text{LO}} + E_{\text{RX}}|$.

Under the weak-probe, steady-state, and near-resonant conditions, $\rho_{11} \simeq 1$, $\rho_{22}, \rho_{33}, \rho_{44} \simeq 0$, $\Delta_{\text{p}} = \Delta_{\text{c}} = 0$, and $\Delta_{\text{RF},k} \approx 0$. Here, γ_{21}, γ_{31}, and γ_{41} denote the effective decoherence rates of the corresponding coherences. Eliminating the upper-state coherence gives

$$\rho_{41} = \frac{\mathrm{j}\Omega_{\text{tot}}}{2\gamma_{41}}\rho_{31}, \qquad \gamma_{31,\text{eff}} = \gamma_{31} + \frac{\Omega_{\text{tot}}^2}{4\gamma_{41}}.$$

Solving the remaining steady-state coherence equations then yields

$$\rho_{21} = \frac{\mathrm{j}\Omega_{\text{p}}/2}{\gamma_{21} + \dfrac{\Omega_{\text{c}}^2}{4\gamma_{31,\text{eff}}}}.$$

Because the probe response is determined by $\mathrm{Im}(\rho_{21})$, the RF-induced baseline-subtracted response satisfies

$$\begin{aligned}\Delta S(\Omega_{\text{tot}}) &\propto \mathrm{Im}[\rho_{21}(\Omega_{\text{tot}}) - \rho_{21}(0)] \propto \frac{\Omega_{\text{tot}}^2}{\Omega_{\text{tot}}^2 + \Gamma_{\text{coh}}^2}, \\ \Gamma_{\text{coh}}^2 &= 4\gamma_{31}\gamma_{41} + \frac{\gamma_{41}}{\gamma_{21}}\Omega_{\text{c}}^2.\end{aligned} \tag{33}$$

Equation (33) directly establishes the quadratic weak-RF dependence and strong-RF saturation of the optical response. The reduced scale Γ_{coh} is introduced only to establish the physical origin of the rational form and is not directly identified with the experimentally calibrated parameter Γ below.

In practice, three coupled mechanisms make this linearization imperfect over a wide synthesized band. The intrinsic nonlinearity of $\mathcal{S}_k(\cdot)$ causes amplitude-dependent gain compression. The optimal working point varies with the addressed Rydberg transition because the dipole moment scales approximately as n^2, and the far-detuned AC-Stark tuning field changes $\Delta_{\text{RF},k}$ and can also modify the effective linewidth through power broadening and thermal averaging. If left uncompensated, these effects distort the I/Q amplitudes and may introduce frequency-dependent phase bias through unequal nonlinear compression in the two quadratures, ultimately degrading the range estimate that relies on the phase evolution across $\{f_k\}$.

A direct remedy would be to compute $\mathcal{S}_k(\cdot)$ from (4) with all experimental parameters and then invert it point-by-point. Although rigorous, this approach is impractical for real-time calibration because numerical integration of the density-matrix dynamics is computationally expensive, accurate values of atomic/laser/environmental parameters are difficult to obtain, and nonideal effects in thermal vapor cells can make first-principles predictions mismatched to the measured response. We therefore adopt an analytical approximation that preserves physical interpretability while being simple enough to calibrate and invert efficiently. In the quasi-static regime, the Lindblad dynamics (4)–(5) define a steady-state mapping from the RF drive to the probe transmission through ρ_{21} and (14)–(15). Under the intended operating condition with $\Delta_{\text{p}} = \Delta_{\text{c}} = 0$

and $\Delta_{\mathrm{RF},k} \approx 0$, the near-resonant RF coupling primarily modifies the EIT/AT feature through an effective broadening and splitting whose scale is set by the composite RF Rabi magnitude $\Omega_{\mathrm{tot}} \propto |E_{\mathrm{LO}} + E_{\mathrm{RX}}|$. After thermal averaging in a vapor cell, finite laser linewidth, and other technical broadenings, the measured dependence of the normalized time-averaged probe transmission on Ω_{tot} becomes smooth and symmetric around the working region, so its dominant behavior can be captured by a two-parameter Lorentzian-type saturation curve. This effective form preserves the key property required for ranging, namely that the small-signal responsivity is the local slope around the LO bias point, while avoiding repeated density-matrix simulations during calibration and compensation.

Accordingly, the baseline-subtracted normalized probe response is represented by the following calibrated Lorentzian-type saturation model:

$$S(\Omega_{\mathrm{tot}}) = A\left(1 - \frac{\Gamma^2}{\Omega_{\mathrm{tot}}^2 + \Gamma^2}\right), \tag{34}$$

where $S(\Omega_{\mathrm{tot}})$ denotes the normalized time-averaged probe response, A is its saturation amplitude, and Γ is the effective characteristic RF-Rabi-frequency scale of the measured nonlinear response.

For an ideal homogeneous four-level model under the weak-probe, steady-state, and resonant conditions, the analytical treatment gives [9]

$$A = \frac{\alpha\gamma_{21}\Omega_{\mathrm{p}}}{\gamma_{21}^2 + 2\Omega_{\mathrm{p}}^2},$$

where γ_{21} is the effective decoherence rate of the optical coherence and α collects the atomic-density, transition-dipole, optical-path, and response-normalization factors. In the same ideal model,

$$\Gamma = \frac{2\sqrt{2}\,\Omega_{\mathrm{p}}}{\sqrt{\Omega_{\mathrm{c}}^2 + \Omega_{\mathrm{p}}^2}}\,\Gamma_{\mathrm{EIT}},$$
$$\Gamma_{\mathrm{EIT}} = \frac{\Omega_{\mathrm{c}}^2 + \Omega_{\mathrm{p}}^2}{2\sqrt{\gamma_2^2 + 2\Omega_{\mathrm{p}}^2}}, \tag{35}$$

where γ_2 is the effective decoherence parameter of the intermediate state. These ideal expressions establish the physical parameter dependence of the model. In the present thermal-vapor implementation, Doppler averaging, finite laser linewidths, additional decoherence, AC-Stark-induced spectral modification, optical losses, and photodetection gain alter the measured amplitude and characteristic scale. Therefore, A and Γ are treated as effective parameters and calibrated experimentally under the corresponding operating conditions.

The responsivity follows directly by differentiating (34):

$$\kappa(\Omega_{\mathrm{tot}}) = \frac{\partial S}{\partial \Omega_{\mathrm{tot}}} = \frac{2A\Gamma^2\Omega_{\mathrm{tot}}}{(\Omega_{\mathrm{tot}}^2 + \Gamma^2)^2}. \tag{36}$$

Setting $\partial\kappa/\partial\Omega_{\mathrm{tot}} = 0$ gives the optimal operating point $\Omega_{\mathrm{tot}} = \Gamma/\sqrt{3}$. This directly explains why the LO power must be carefully chosen: too weak an LO reduces the slope and degrades sensitivity, whereas too strong an LO pushes the receiver into a compressed region where the slope decreases and higher-order nonlinearities become prominent. Over a synthesized wide band, the effective Ω_{tot} at the cell varies with frequency because the selected Rydberg transition changes the dipole matrix element and because the AC-Stark tuning field modifies the operating point through $\Delta_{\mathrm{RF},k}$. Consequently, a fixed LO setting cannot maintain a constant κ_k across all f_k, and the raw I/Q samples extracted from the photodetector are not directly comparable across the grid.

To obtain a computationally efficient compensation rule that remains physically grounded, we calibrate a Lorentzian-type response function in the vicinity of the optimal LO at each operating configuration. The calibration uses three experimentally accessible quantities at the maximum-slope point: the corresponding composite Rabi frequency $\Omega_{\max}$, the signal value $S_{\max} = S(\Omega_{\max})$, and the maximum gain $\kappa_{\max} = \kappa(\Omega_{\max})$. The quantity $\Omega_{\max}$ is determined from the AT splitting of the EIT spectrum, where the measured peak separation Δf provides an SI-traceable estimate of the RF coupling strength. The linewidth parameter follows from the extremum condition of (36), yielding $\Gamma = \sqrt{3}\,\Omega_{\max}$, and the amplitude factor is obtained as $A = 8\kappa_{\max}\Omega_{\max}/3$. Substituting these relations into (34) yields a calibrated nonlinear response around the working region written as

$$S(\Omega_{\mathrm{tot}}) = \frac{8\kappa_{\max}\Omega_{\max}\Omega_{\mathrm{tot}}^2}{3(\Omega_{\mathrm{tot}}^2 + 3\Omega_{\max}^2)} + S_{\max} - \frac{2\kappa_{\max}\Omega_{\max}}{3}, \tag{37}$$

which captures the dominant nonlinearity without requiring repeated density-matrix simulations. Because (37) is monotonic in Ω_{tot} over the operating region, it admits an efficient inverse mapping $S^{-1}(\cdot)$ that converts a measured probe signal back to an equivalent composite Rabi frequency, enabling real-time linearization. The compensation is applied to the time-averaged mixed outputs $(\bar{I}_k, \bar{Q}_k)$ and to the corresponding LO-only reference outputs $(I_{\mathrm{LO},k}, Q_{\mathrm{LO},k})$ to remove both the nonlinear distortion and the LO background, producing the compensated quadratures denoted as

$$I_k = S^{-1}(\bar{I}_k) - S^{-1}(I_{\mathrm{LO},k}), \tag{38}$$
$$Q_k = S^{-1}(\bar{Q}_k) - S^{-1}(Q_{\mathrm{LO},k}). \tag{39}$$

After applying (38)–(39), the compensated I/Q samples satisfy the linear homodyne ranging model (23)–(24) with a stabilized effective responsivity across the stepped-frequency grid, thereby mitigating frequency-dependent gain compression and the associated phase distortions that would otherwise corrupt one-dimensional ranging. In addition, (35) implies that when the coupling-Rabi-frequency variation across the grid satisfies $\Delta\Omega_{\mathrm{c}} \ll \Omega_{\mathrm{p}}$, the resulting Γ is approximately proportional to Γ_{EIT}, so a single calibration of this proportionality constant can be reused to rapidly determine near-optimal LO settings across multiple frequency points, which simplifies multi-frequency operation under AC-Stark tuning.

C. Ranging Algorithm for Rydberg Atomic Homodyne Receivers

After obtaining the compensated quadratures via (38)–(39), each stepped-frequency point f_k provides a complex baseband sample $s_k = \hat{I}_k + \mathrm{j}\hat{Q}_k$ whose phase carries the propagation delay information. In an ideal dense-sampling SFCW radar, one could directly apply a non-uniform Fourier transform (NUFFT) across $\{f_k\}$ to form a range profile. In the present quantum-receiver setting, however, two practical constraints motivate a reconstruction method that is robust to both undersampling and non-Gaussian perturbations. First, the frequency grid $\{f_k\}_{k=1}^{K}$ is fundamentally constrained by quantum-state-selective reception and tuning, so the number of usable sampling points K can be far smaller than that required by conventional matched filtering to suppress sidelobes and grating lobes. Second, unlike conventional coherent receivers, where mixing is implemented using an electronic multiplier, the LO field in a Rydberg receiver propagates through free space and may undergo multipath reflections. Together with technical noise sources, these effects can introduce outlier components that deviate from the Gaussian assumption typically used in standard least-squares ranging.

To make the reconstruction problem explicit, we discretize the range axis on a grid $\mathbf{r} = [r_1, \ldots, r_{N_r}]^T$ and represent the reflectivity profile on that grid by $\mathbf{x} \in \mathbb{C}^{N_r}$. The compensated measurements across the non-uniform grid are collected into a vector $\mathbf{s} = [s_1, \ldots, s_K]^T \in \mathbb{C}^K$. Under the single-scatterer or sparse-multipath assumption, the ranging model can be written in the standard linear form

$$\mathbf{s} \approx \mathbf{\Phi}\mathbf{x} + \mathbf{w}, \tag{40}$$

where $\mathbf{w}$ denotes the aggregate residual noise after preprocessing, and the measurement matrix $\mathbf{\Phi} \in \mathbb{C}^{K \times N_r}$ is constructed as

$$\mathbf{\Phi}(k, n) = \exp\left(-\mathrm{j}\frac{4\pi f_k r_n}{c}\right). \tag{41}$$

Here c is the speed of light. Deterministic phase terms that are independent of target range (such as stable hardware delays and fixed reflection/branch offsets) are treated as calibration factors and are removed in preprocessing, so that (41) captures only the propagation-induced phase progression versus f_k. With this formulation, one-dimensional ranging reduces to estimating $\mathbf{x}$ from $\mathbf{s}$ given a potentially sub-Nyquist number of frequency samples K.

The key reason for adopting compressive sensing is that, under sparse scenes, $\mathbf{x}$ is approximately sparse on the range grid, while the mapping (40) remains linear. In our controlled ranging experiments, the scene is sparse, and the non-uniform frequency sampling imposed by quantum-state selection leads to strong sidelobes and spurious peaks when directly applying NUFFT methods under limited K. By enforcing sparsity, compressive sensing suppresses the undersampling artefacts that would otherwise obscure the true peaks, thereby improving robustness and peak detectability under the current sampling constraints. When the scene is not sparse, conventional dense sampling or alternative regularized inversions would be more appropriate. The CS-Rydberg formulation is therefore targeted at sparse ranging scenarios and at regimes where the number of frequency points is limited by the current prototype implementation.

In addition to undersampling, robustness to outliers is critical. The preprocessing stage in Algorithm 1 first applies

Algorithm 1 CS-Rydberg Ranging Algorithm

Require: Non-uniform frequency grid $\{f_k\}_{k=1}^{K}$
Require: I/Q signals $\mathbf{I}, \mathbf{Q} \in \mathbb{R}^{K \times N_s}$
Require: LO reference $\mathbf{I}_{\text{LO}}, \mathbf{Q}_{\text{LO}} \in \mathbb{R}^{K \times N_s}$
Require: Range grid $\mathbf{r} = [r_1, \ldots, r_{N_r}]^T$
Require: Huber param δ, tolerance ϵ
Ensure: Range profile $\mathbf{p}_{\text{CS}}$

$\mathbf{s} \leftarrow \text{zeros}(K)$ *// Initialize signal vector*
for $k \leftarrow 1$ **to** K **do**
  $\tilde{I}_k \leftarrow \text{medfilt}(I_k, 50)$ *// Median filter (impulse noise)*
  $\tilde{Q}_k \leftarrow \text{medfilt}(Q_k, 50)$
  $\bar{I}_k \leftarrow \text{mean}(\tilde{I}_k)$ *// Temporal averaging*
  $\bar{Q}_k \leftarrow \text{mean}(\tilde{Q}_k)$
  $\bar{I}_{\text{LO},k} \leftarrow \text{mean}(I_{\text{LO},k})$
  $\bar{Q}_{\text{LO},k} \leftarrow \text{mean}(Q_{\text{LO},k})$
  // Nonlinear compensation (S^{-1})
  $\hat{I}_k \leftarrow S^{-1}(\bar{I}_k) - S^{-1}(\bar{I}_{\text{LO},k})$
  $\hat{Q}_k \leftarrow S^{-1}(\bar{Q}_k) - S^{-1}(\bar{Q}_{\text{LO},k})$
  $s_k \leftarrow \hat{I}_k + \mathrm{j}\hat{Q}_k$
  $\mathbf{s}[k] \leftarrow s_k$
end for
$\mathbf{\Phi} \leftarrow \text{BuildMeasurementMatrix}(f_k, r_n)$ *// Eq.(41)*
$\mathbf{x} \leftarrow \text{SolveOptimization}(\mathbf{\Phi}, \mathbf{s}, \delta, \epsilon)$ *// Eq.(42)*
$\mathbf{p}_{\text{CS}} \leftarrow |\mathbf{x}|$
$\mathbf{p}_{\text{CS}} \leftarrow \mathbf{p}_{\text{CS}} / \max(\mathbf{p}_{\text{CS}})$ *// Normalization*
return $\mathbf{p}_{\text{CS}}$

median filtering along the samples within each dwell to remove impulsive disturbances, which can arise from occasional LO multipath and measurement glitches. Temporal averaging then increases the effective SNR before nonlinear correction. The nonlinear compensation $S^{-1}(\cdot)$ is applied prior to differencing the LO-only reference because subtraction in the raw detector domain does not commute with the nonlinear atomic response. This step restores a field-proportional quantity and is required for the linear model to be meaningful across the stepped grid. After compensation, we retain the complex samples s_k so that the linear forward model remains valid, and any residual amplitude variation across $\{f_k\}$ is treated as model mismatch and absorbed into $\mathbf{w}$.

The sparse reconstruction is then performed by solving a Huber-regularized constrained optimization

$$\begin{aligned} &\min_{\mathbf{x}} \sum_{n=1}^{N_r} \phi_\delta(|x_n|), \\ &\text{s.t. } \|\mathbf{\Phi}\mathbf{x} - \mathbf{s}\|_2 \le \epsilon, \end{aligned} \tag{42}$$

where ϵ is a noise tolerance and $\phi_\delta(\cdot)$ is the Huber function

$$\phi_\delta(z) = \begin{cases} \dfrac{z^2}{2\delta}, & |z| \le \delta, \\ |z| - \dfrac{\delta}{2}, & |z| > \delta. \end{cases} \tag{43}$$

The Huber penalty is used here as a smooth surrogate that transitions from a quadratic penalty near zero to an ℓ_1-like penalty for larger magnitudes, which provides a convenient sparsity-promoting regularizer for $\mathbf{x}$. The final range profile is obtained as $\mathbf{p}_{\text{CS}} = |\mathbf{x}|$ followed by normalization.

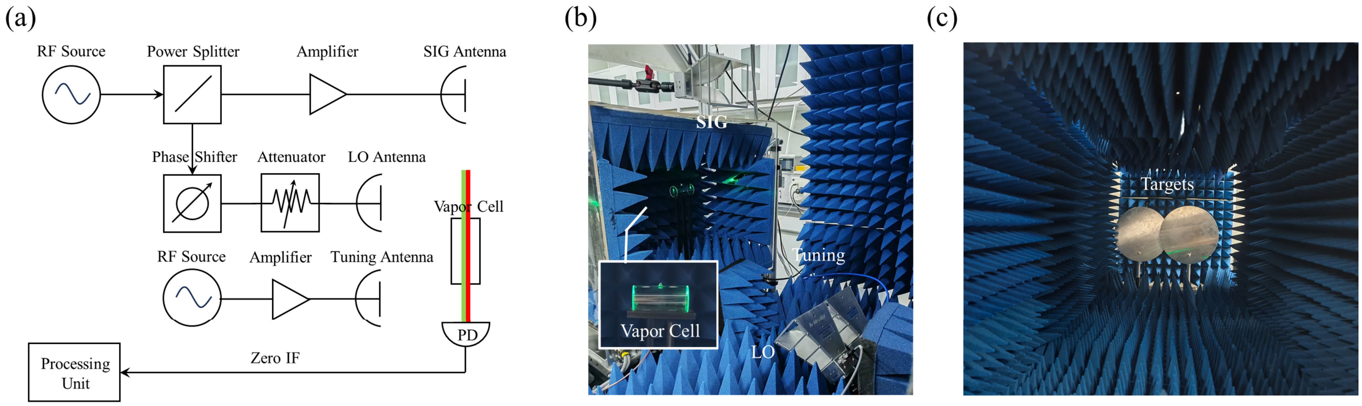

Fig. 2. Overview of experimental radar framework. (a) Rydberg atomic homodyne receiver, (b) and (c) experimental setup. The SIG field and LO field are generated from the same RF source to maintain long-term phase coherence and power-split. The SIG field is amplified by an amplifier and transmitted toward the target via a horn antenna. The LO field passes through a phase shifter to adjust its initial phase difference relative to the SIG field, and is then optimized in amplitude via an attenuator before propagating toward the atomic vapor cell through another horn antenna. The tuning field is generated by a separate RF source and directed toward the vapor cell. On the receiver side, the probe laser and coupling laser counter-propagate and overlap through the vapor cell, and their transmitted lasers are collected by photodetector and recorded by oscilloscope. In the experimental setup, the targets are two 400 mm diameter aluminum circular plates mounted on displacement stages with a 500 mm travel range.

TABLE II
RYDBERG TRANSITION FREQUENCIES AND MEASURED PARAMETERS

Rydberg States	Tuning (+/-) Field	Theoretical Frequency (GHz)	Measured Frequency (GHz)
$64D_{5/2}$	-	2.625	2.640
$63D_{5/2}$	-	2.757	2.766
$62D_{5/2}$	-	2.899	2.912
$61D_{5/2}$	-	3.050	3.063
$60D_{5/2}$	-	3.212	3.225
$59D_{5/2}$	-	3.386	3.398
$59D_{5/2}$	+	/	3.499
$58D_{5/2}$	-	3.565	3.584

IV. EXPERIMENTAL RESULTS

A. Experiment Implementations

The primary element of the system is a cylindrical Cs-133 vapor cell measuring 5 cm in length and 2.5 cm in diameter. Experiments are performed in a microwave anechoic chamber to mitigate environmental electromagnetic interference and multipath effects. Fig. 1(b) and Fig. 2 (b) and (c) demonstrate that a 852 nm probe laser excites atoms from the ground state $6S_{1/2}$ to the intermediate state $6P_{3/2}$, with its frequency stabilised through saturated absorption spectroscopy. A 509 nm coupling laser excites atoms to Rydberg states with principal quantum numbers ranging from $n = 58$ to 64. The probe and coupling lasers propagate in opposite directions and overlap within the vapor cell to reduce Doppler broadening. The probe laser functions at a power of 50 μW and has a beam waist of approximately 1.0 mm, whereas the coupling laser operates at 30 mW with a beam waist of around 1.3 mm. Both lasers feature linewidths below 1 MHz, and their beams are aligned to overlap near the center of the vapor cell in a counter-propagating configuration. The coupling laser's dynamic frequency tuning is accomplished through mechanical adjustments of the piezoelectric actuator in the laser's external cavity, enabling selective alignment with Rydberg transitions at S-band frequencies. The transitions utilised in the experiments are presented in Table II. The measured transition frequencies are calibrated prior to each experiment and may exhibit slight deviations from nominal values. These shifts are primarily attributed to the AC-Stark effect induced by the strong coupling laser and LO fields, as well as residual laser locking offsets. We compensate these systematics by using in-situ calibrated frequencies during signal synthesis, which largely removes the apparent shifts. The maximum frequency interval between adjacent steps is 173 MHz, corresponding to a maximum unambiguous radar range of approximately 0.87 m.

The stepped-frequency waveform is synthesized by a vector signal generator (1466H-V, Ceyear) with 8 non-uniform frequency steps. These frequencies are initially calculated using the Alkali Rydberg Calculator (ARC) [31] and experimentally calibrated to ensure resonance. For each target frequency, we first estimate the required AC-Stark shift using ARC and then experimentally fine-tune the tuning-field intensity around the theoretical estimate to maximize the homodyne readout response at that frequency. Under stable system conditions, the dwell time of each frequency step does not affect one-dimensional range profiling. Thus, dwell times are maximized to ensure frequency and power stability after laser retuning. As shown in Fig. 2(a), both the SIG field and LO field are generated by the same vector signal generator and split via a power divider to maintain a common time reference and LO coherence over extended periods. The signal path is amplified and transmitted toward the target via a horn antenna. The LO path passes through a voltage-controlled phase shifter to generate in-phase and quadrature components, followed by an attenuator to optimize LO power levels across frequency steps. A far-detuned RF field (2 GHz), generated by a secondary RF source, operates at frequencies far from the Rydberg resonance. High-frequency electric field tuning is adopted to avoid low-frequency shielding effects caused by Rydberg atom adsorption on the vapor cell walls, which would otherwise induce standing waves and phase measurement errors in homodyne detection. This approach also mitigates insertion loss variations from phase shifter and attenuator adjustments. All three RF fields (SIG, LO, and tuning fields) employ identical linearly polarized antennas (LB-20180-SF), with the LO polarization aligned parallel to the coupling laser polarization. These broadband horns feature a frequency-dependent 3-dB beamwidth of E-plane 85 °–19 ° and H-plane 77 °–18 ° over 2–18 GHz. Geometrically, the SIG antenna is boresighted toward the target to maximize illumination, while the LO antenna is boresighted toward the vapor cell. In both paths, the target and cell are positioned within the antenna main lobe to ensure a well-defined RF incidence geometry. The horn antenna has a maximum aperture dimension of 13 cm, yielding a far-field boundary distance of approximately 23 cm at 2 GHz. The reason for employing a high-frequency electric field for continuous frequency tuning, rather than a magnetic field [32] or a DC electric field [33], is that devices placed in close proximity to the vapor cell tend to reflect electromagnetic waves. Such reflections exacerbate insertion-loss variations during phase-shifter adjustments, thereby increasing phase-measurement errors. Additionally, the LO field path maintains a distance of 45 cm from the vapor cell to ensure far-field conditions. The echo signal modulates the Rydberg atomic energy levels, altering the transmission intensity of the probe laser. This perturbation is down-converted to the DC baseband through homodyne detection, captured by a photodetector (PDA36A2, Thorlabs), and recorded using a digital oscilloscope (Tektronix MSO56B). Two aluminum circular plates (diameter: 400 mm) serve as ranging targets, mounted on parallel displacement stages to provide adjustable distances. The absolute distance is measured from the antenna aperture plane using a laser rangefinder (±3 mm accuracy). The measured distance consists of three segments: R_1, the distance from the aperture of the SIG antenna to the target, R_2, the distance from the target to the region where the laser beams overlap, and D, the distance from the aperture of the LO antenna to the target. The target range is then defined as $R = 1/2(R_1 + R_2 - D)$, which cancels the phase shift induced by the vapor-cell medium and corrects for any offset between the antenna phase center and the mechanical reference.

Pre-experimental calibration of the optimal LO power is based on the method in Section III-B by adjusting the attenuator of the LO path. Resonant frequencies at optimal power are individually determined to account for AC-Stark shifts caused by the LO field, ensuring optimal alignment of atomic transitions across the frequency steps. Additionally, the orthogonality of the I/Q components is calibrated using a vector network analyzer (Ceyear 3657A), recording the phase shifter input voltages corresponding to 0° and 90° phase differences between the LO and SIG fields. The frequency-dependent insertion losses of the SIG and LO RF chains were also characterized using the VNA, and the attenuation settings were adjusted at each frequency step so that the powers referred to the horn-input planes were maintained at approximately -10 dBm for the SIG path and -6 dBm for the LO path. To ensure phase stability, electronic components and cables (bending-induced phase variation $\leq 0.1°/\mathrm{GHz}$) are rigidly fixed to minimize mechanical disturbances during operation.

To isolate the contribution of each processing module under the same severe sampling constraint as the experiment, we additionally perform a simulation-based ablation study with parameters tied to the measured system. We use the same $K = 8$ non-uniform carrier set $\{f_k\}$ as in Table II (effective bandwidth $B = f_{\max} - f_{\min} \approx 0.94$ GHz), and reconstruct the range profile on a grid $r_n \in [0, 5]$ m. Following the signal model in Sec. III, the per-tone complex measurement vector $\mathbf{s} \in \mathbb{C}^K$ is formed from the simulated I/Q baseband outputs after the same preprocessing chain, and the sensing matrix $\mathbf{\Phi} \in \mathbb{C}^{K\times N}$ is constructed as $\Phi(k, n) = \exp(-j4\pi f_k r_n/c)$. The scene consists of a dominant reflector at $R_{\text{true}} = 2.0$ m and a weak delayed multipath component at $R_{\text{mp}} = 2.2$ m with amplitude ratio $\alpha = 0.30$. Correlated per-tone phase jitter is modeled as an AR (1) process ($\rho = 0.92$, $\sigma_{\text{corr}} = 0.20$ rad, $\sigma_{\text{iid}} = 0.05$ rad). Impulsive disturbances are included by adding spike outliers with probability $p_{\text{spk}} = 0.20$ and amplitude $A_{\text{spk}} = 1.10$ (normalized units), in addition to Gaussian noise with standard deviation $\sigma = 0.01$. Monte Carlo statistics are obtained from $N_{\text{MC}} = 250$ trials.

B. Experimental Results

Fig. 3 (a) shows the measured probe transmission as a function of the applied RF electric field under four conditions: 1) no RF, 2) LO only, 3) signal + LO in-phase, and 4) signal + LO in quadrature. The transmission curves highlight the response of the Rydberg receiver. In the absence of any RF (no RF), the probe laser transmission remains at its baseline level (the natural EIT transmission with no perturbing field). With only the LO field applied, the transmission shifts due to the AT-splitting from the LO, establishing a bias point on the atomic resonance. When an echo signal is added in-phase (0° out of initial phase with the LO), the total RF field amplitude increases. Conversely, adding the signal in quadrature (90° out of initial phase with the LO) produces a larger net change in transmission. This is because, under these conditions, the echo signal undergoes stronger cross-interference with the LO, resulting in a larger perturbation of the atomic medium and a more pronounced change in transmission. The in-phase and quadrature outputs can be used to reconstruct the echo signal incident on the atomic vapor cell. Using the LO-background-subtracted I/Q data, the coherent amplitude and combined RMS noise were evaluated as $A_{\text{s}} = \sqrt{\Delta I^2 + \Delta Q^2}$ and $\sigma_{\text{n}} = \sqrt{\sigma^2_{I,\text{SIG+LO}} + \sigma^2_{Q,\text{SIG+LO}} + \sigma^2_{I,\text{LO}} + \sigma^2_{Q,\text{LO}}}$, respectively, yielding a pre-reconstruction baseband SNR of $20\log_{10}(A_{\text{s}}/\sigma_{\text{n}}) \approx 24.4$ dB at 3.225 GHz. Fig. 3(b) shows the variation of the spectral transmission under resonant conditions as a function of the applied electric field strength. The experimental data (markers) are in excellent agreement with the theoretical EIT-based model (solid curves), which predicts a saturating response as the RF field increases. Deviations between experiment and theory grow progressively at very low and very high fields, owing to AC-Stark-induced shifts in the resonance frequency, which detune the probed transition from resonance. The inset depicts the spectrum recorded at the optimal LO bias. Compared with the results reported in [9] and [34], the corresponding field values shown here are

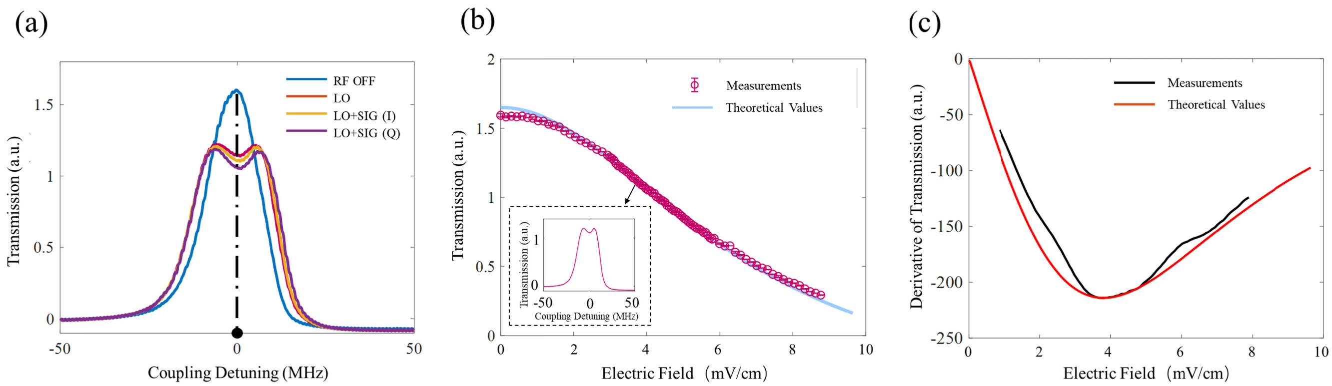

Fig. 3. Experimental demonstration of the Rydberg atomic receiver and its nonlinear response principle. (a) Spectra under conditions of no RF field (blue curve), LO field only (red curve), in-phase LO and SIG fields (yellow curve), and quadrature-phase LO and SIG fields (purple curve). The transmission value at resonance is taken as the output of the Rydberg atomic receiver. (b) Transmission versus electric field under resonant conditions. Experimental data are shown as red circles. Error bars represent 1σ standard errors obtained from 3 measurements. The blue curve shows theoretical calculations based on Eq. (37). The inset displays the AT splitting spectrum under optimal LO conditions and its position in the transmission-electric field relation. (c) Intrinsic gain coefficient of the Rydberg atomic receiver versus electric field strength. The black curve is the derivative of interpolated experimental data from (b) after Gaussian smoothing. The red curve shows the derivative of the theoretical curve in (b) according to Eq. (36).

smaller, likely due to additional Doppler-broadening effects. Crucially, the derivative of the transmission with respect to the electric field, also shown in Fig. 3(c), illustrates the receiver's gain. This derivative ($\mathrm{d}T/\mathrm{d}E$) peaks at an intermediate field amplitude, indicating an optimal operating point where the atomic medium is most sensitive to small changes in E. At low fields, the slope is initially small (the atoms are in the linear regime of response). As the LO bias raises the operating point, the slope increases, reaching a maximum gain where the system responds most strongly to the signal. Beyond this point, the slope decreases, as the Rydberg atoms saturate and additional field produces diminishing changes in transmission. This gain saturation is a direct consequence of the atomic population approaching the upper state limit (once a significant fraction of atoms are already excited by the combined LO+SIG field, the transparency can no longer change linearly with further field increase). Physically, this behavior mirrors a classical receiver's amplifier saturation, manifested in the optical domain via EIT. From this fit, one can extract an estimated maximum incremental gain of the atomic receiver. For example, the peak derivative corresponds to a gain of approximately 213 a.u. of transmission per V/m (arbitrary units), achieved at an RF field around $E \approx 3.7$ mV/cm. This confirms that the receiver operates optimally in a certain field range, and outside this range, sensitivity drops.

After determining the receiver's amplitude response, we proceed to assess its capability to accurately measure RF phase. In a homodyne system, the output is contingent upon the phase difference between the SIG and LO, expressed as $V_{\text{out}} \propto \cos(\Delta\phi)$ for the in-phase channel, while the quadrature channel exhibits a $\sin(\Delta\phi)$ dependence. The LO phase is incrementally adjusted in steps of $\pi/6$, maintaining a constant signal amplitude for testing purposes. The output of the receiver, indicating changes in optical transmission, is recorded for each relative phase. The nonlinear amplitude response of the atomic sensor, illustrated in Fig. 4, necessitates the application of a calibration curve or nonlinear compensation to transform the raw transmission changes into a linearised output

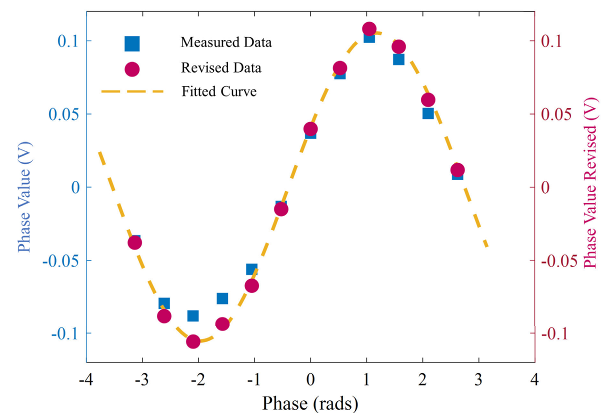

Fig. 4. Internal phase-readout calibration under a controlled LO phase sweep. Blue squares show the raw demodulated output of the Rydberg-atomic homodyne receiver as the LO phase is stepped in $\pi/6$ rad increments at a fixed signal amplitude. Red circles indicate the output revised by the nonlinear response of Eq. (36). The yellow dashed curve corresponds to a cosine function fitted to the red circles, with $R^2 = 99.89\%$.

that is proportional to the effective RF field. Fig. 4 illustrates the normalised receiver output in relation to the LO phase shift following the compensation process. The data points closely align with a cosine function, represented by the solid fitted curve. The cosine fit exhibits a coefficient of determination $R^2 = 99.89\%$, signifying a nearly perfect alignment with the anticipated cos relationship. This illustrates two significant aspects: 1) The Rydberg receiver exhibits a repeatable relative-phase dependence under controlled LO phase sweeps, and 2) the in-phase and quadrature components of the signal are appropriately orthogonal and balanced. The LO phase sweep results in a cosinusoidal variation of the in-phase channel output, with no leakage of the quadrature component. A 90° phase shift in the LO causes the receiver output to traverse the complete sinusoidal cycle, indicating the existence of a corresponding quadrature channel if measured. The near-unity R^2 and the lack of distortion in Fig. 4 indicate that the atomic

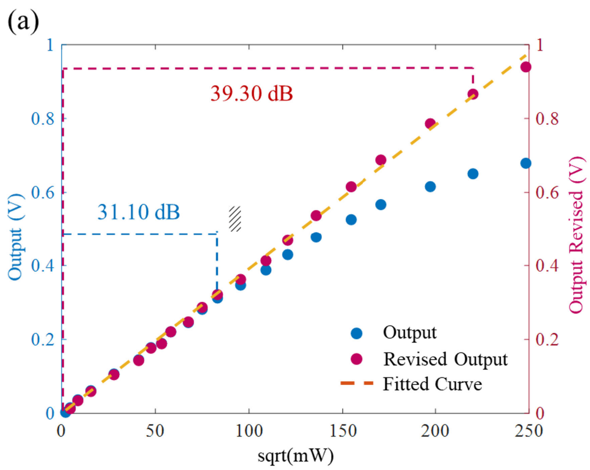

Fig. 5. Linearity and dynamic range of the Rydberg atomic homodyne receiver under: (a) coherent enhancement, and (b) coherent cancellation conditions. Blue circles represent the raw demodulated output, red circles represent the output after nonlinear compensation, and the yellow dashed line is a linear fit to the small-signal regime. In (a), the uncorrected linear dynamic range is 31.10 dB, extending to 39.30 dB after compensation. In (b), it is 30.00 dB uncorrected and 37.24 dB with compensation. In both cases, a dynamic range improvement of over 7 dB is achieved after nonlinear compensation.

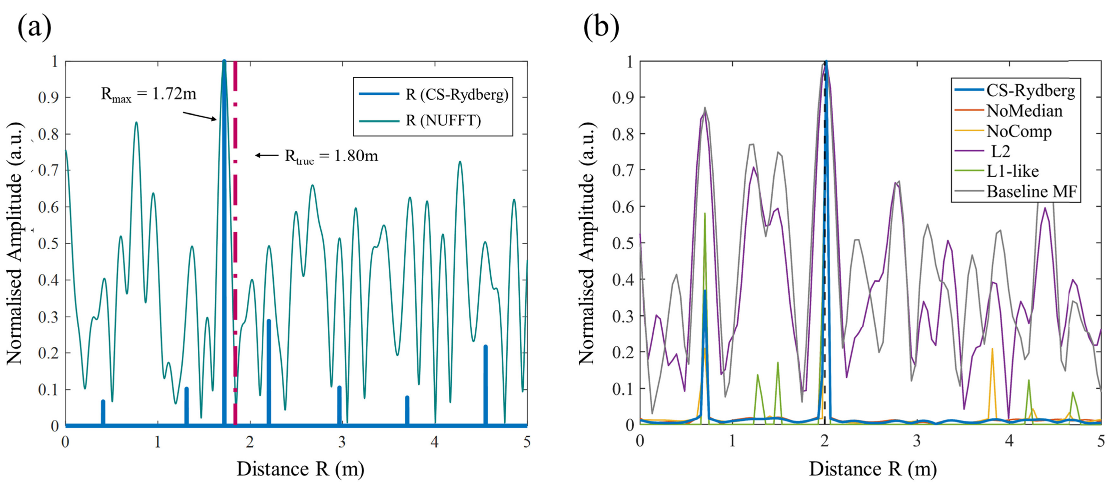

Fig. 6. Performance analysis of the proposed signal processing framework. (a) One-dimensional range profile comparison showing that the proposed CS-Rydberg algorithm (blue curve) significantly suppresses sidelobes and artifacts compared to the conventional NUFFT method (green curve). (b) Ablation study revealing the contribution of each processing stage. The full CS-Rydberg framework (orange curve) is compared against configurations omitting median filtering (NoMedian), omitting nonlinearity compensation (NoComp), using L1-like regularization, and the baseline matched filter (MF). This validates that both preprocessing and nonlinearity compensation are critical for high-quality reconstruction.

mixer functions as an ideal IQ demodulator for small signals, effectively converting the RF field's phase into a measurable optical output. Minor deviations from the ideal cosine, with data points closely aligning to the fitting curve and maximum deviations less than 1%, can be ascribed to experimental uncertainties, including residual amplitude modulation and inadequate compensation for the nonlinear response. These results confirm that phase coherence is preserved during the atomic detection process, with the interference between the LO and SIG within the vapor cell producing a stable and repeatable phase-dependent output. This capability is essential for applications such as interferometric sensing or coherent radar, as it allows the Rydberg receiver to operate similarly to a traditional coherent detector, delivering both amplitude and phase information of the RF field.

Fig. 5 evaluates the receiver's linearity and dynamic range by plotting the demodulated output V_{out} versus equivalent input voltage under two phase conditions: (a) coherent enhancement of the SIG field with the LO field, and (b) coherent cancellation. In both instances, the LO field is maintained at a high-sensitivity bias point, while the SIG field, calibrated using a vector network analyzer, is varied from the system noise floor to saturation. In the small-signal regime, both the raw output and the predistorted output align with a yellow dashed linear fit, confirming that $V_{\text{out}} \approx \kappa E_{\text{sig}}$. Outside this region, the slope diverges from the reference line as a result of atomic-saturation-induced compression, and at elevated inputs, the output approaches a plateau. The coherent-enhancement case shows that the uncorrected linear dynamic range is approximately 31.10 dB, which increases to 39.30 dB after nonlinear compensation, resulting in a gain of 8.20 dB. In the coherent-cancellation scenario, the initial range is approximately 30.00 dB, which increases to 37.24 dB with compensation, resulting in a 7.24 dB enhancement.

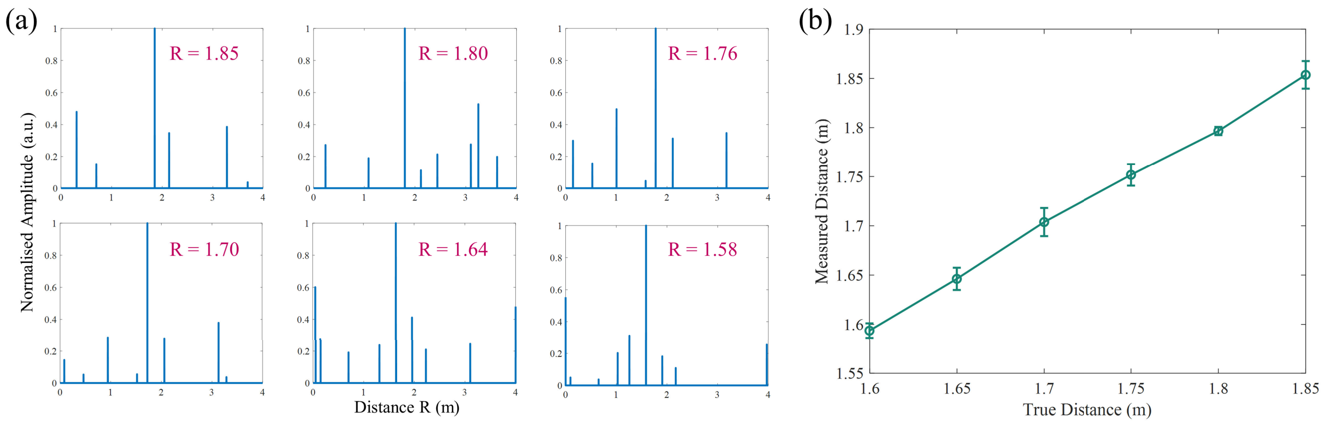

Fig. 7. Single-target relative displacement and ranging repeatability experimental results. The target plate is translated on a motorized stage from 1.60 m to 1.90 m in 0.05 m increments. A reference measurement at 1.90 m is used once to estimate and remove a constant range-origin bias introduced by static system delays, and the same offset is applied to all other distances. (a) Ranging results for six target positions in a single measurement run, and (b) Summary of five independent measurement runs. The horizontal axis denotes the true target distance, and the vertical axis shows the ranges measured by the radar system based on Rydberg atomic homodyne receiver. Error bars represent $\pm 1\sigma$ standard error from five measurements. The system achieves a root mean squared error (RMSE) of 1.06 cm and maximum measurement deviation of 2.3 cm.

TABLE III
ABLATION RESULTS

Case	MAE (cm)	RMSE (cm)	PSLR (dB)	MaxSide	FP	Hit
CS-Rydberg	2.13	2.45	5.33	0.27	0.00	1.00
NoMedian	6.95	32.25	2.53	0.32	0.03	0.98
NoComp	2.37	2.79	4.57	0.29	0.00	1.00
ℓ_2	9.41	36.57	0.25	0.85	0.77	0.96
ℓ_1-like	2.44	5.23	3.96	0.36	0.00	1.00
Baseline MF	2.31	2.69	0.64	0.85	0.80	1.00

Consequently, compensation increases the usable dynamic range by over 7 dB in both scenarios, encompassing over two orders of magnitude in input amplitude. The lower limit of each range is determined by the system's noise floor, primarily influenced by laser noise, detector noise, and atomic projection noise, which establishes the minimum detectable signal.

Following the characterization of the receiver's baseband performance, radar ranging experiments were performed to assess its practical capabilities using a straightforward bistatic configuration, where the Rydberg atomic receiver detects echoes from a metal plate positioned at approximately 1.80 m. All reported distances correspond to the averaged two-way path lengths post-processing, with the LO propagation distance subtracted. Fig. 6(a) illustrates the one-dimensional range profile, where the conventional NUFFT method (green curve) reveals a primary peak at 1.72 m. While the peak width aligns with the theoretical resolution of 15 cm, the slight ranging offset arises from effective phase-center drift and cumulative path errors. More critically, the profile suffers from significant spurious peaks due to insufficient frequency sampling and multipath effects. In contrast, the CS-Rydberg algorithm (blue curve) effectively suppresses these undersampling artifacts, improving target clarity. To rigorously validate the processing architecture, Fig. 6(b) and Table III present an ablation study analyzing metrics such as Mean Absolute Error (MAE), Root-Mean-Square Error (RMSE), and Peak-to-Sidelobe Ratio (PSLR). The quantitative results demonstrate that CS-Rydberg substantially outperforms the matched-filter baseline. Specifically, removing the median prefilter increases vulnerability to impulsive disturbances (resulting in large RMSE), while omitting nonlinearity compensation degrades the profile by elevating sidelobes. Furthermore, replacing the sparsity promotion with an ℓ_2 penalty fails to suppress the sampling artifacts, confirming the necessity of the full proposed framework for robust detection.

Consequently, given the present experimental conditions, validating the ability of Rydberg atoms to conduct direct ranging through absolute phase measurements is not feasible. Ranging is accomplished through a singular calibration process to ascertain the relative positional offset. This study assesses the accuracy and repeatability of relative displacement measurements of a target. A metallic reflector is displaced across seven specified distances, varying from 1.60 m to 1.90 m in increments of 5 cm. Five independent ranging measurements are conducted at each position utilising the Rydberg atomic homodyne receiver. A single reference measurement at 1.90 m is used once to estimate the constant range-origin offset, and the same offset is then applied uniformly to all other distances, rather than adjusting each trace individually. Fig. 7(a) presents the one-dimensional range profiles derived from a single independent set of measurements at six target positions, excluding the calibration point at 1.90 m. Each measurement consistently demonstrates a distinct echo peak at the established target distances. Residual sidelobes and spurious peaks remain because the eight-point non-uniform frequency grid produces a non-ideal range point-spread function, while coherent multipath and LO leakage, together with residual frequency-dependent response and phase-calibration errors, introduce additional model mismatch. Fig. 7(b) illustrates the average measured distance in relation to the actual distance, where each data point denotes the mean of five trials, and error bars represent ± 1 standard deviation. The findings

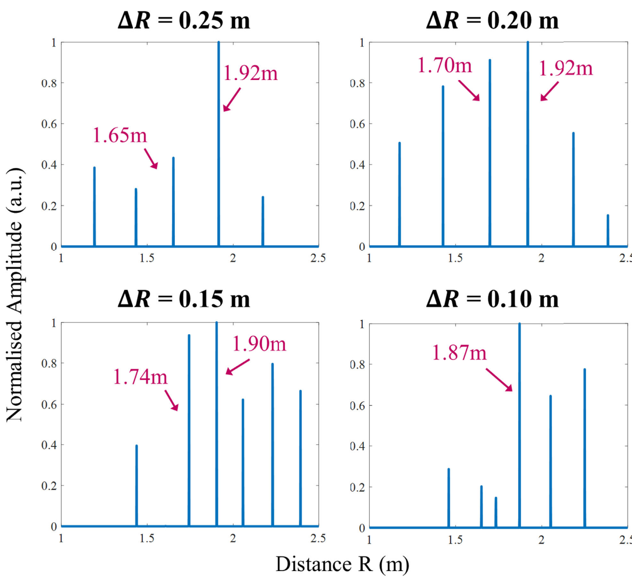

Fig. 8. Dual-target resolution experiment results. Two target plates are placed within the transmit beam and mounted on motorized stages: one plate fixed at 1.90 m, the other translated from 1.65 m to 1.80 m in 5 cm increments. When restricting the ranging window to 1 to 2.5 m, two distinct peaks corresponding to the true target positions are observed for the separation cases of 25 cm, 20 cm and 15 cm. For the separation case of 10 cm, the two peaks merge and are not consistently resolvable under sparsity constraints. This indicates an achievable target separation of 15 cm in sparse scenarios.

demonstrate high measurement accuracy, consistently matching true distances with deviations of less than 3 cm across the full tested range of 1.60 to 1.85 m. The average discrepancy between the measured and true distances is -0.08 cm, suggesting that the system demonstrates minimal systematic bias. The root-mean-square error (RMSE) of the measurements is 1.06 cm. The data presented in Fig. 7 provide strong evidence for the feasibility of utilising quantum sensors in practical remote sensing applications, indicating that measurement capability remains uncompromised by the atomic medium.

We conduct a dual-target resolution test using two metallic reflectors to experimentally verify the range resolution capability of the Rydberg atomic radar. One target is positioned at approximately 1.90 m, while the other is affixed to a movable stage that enables precise adjustments in distance relative to the radar sensor. The movable reflector is initially set at 1.65 m, creating a target separation of 25 cm. The second target is subsequently moved incrementally closer, from 1.65 m to 1.80 m in 5 cm increments. At each distance, a one-dimensional range profile is reconstructed using the CS-Rydberg algorithm. The limited frequency points under the existing experimental conditions, coupled with pronounced multipath effects involving two targets, result in numerous false peaks in the range profile. However, the two target-related peaks that progressively approach one another remain observable, as illustrated in Fig. 8. When the target separation is 15 cm or greater, two distinct and clearly separable peaks consistently emerge, corresponding to the two reflectors. As the separation decreases below 15 cm, the two echoes merge into a single response, preventing the algorithm from distinctly resolving both targets. This indicates that 15 cm is the minimum observable separation in this experiment. However, statistical validation is necessary to confirm a reliable resolution threshold. The observed limit of 15 cm is close to the theoretical resolution of 16 cm, which is facilitated by the synthesised 1-GHz bandwidth. Sparse sampling limits practical resolution from achieving theoretical optimum, whereas the CS-Rydberg algorithm reduces sidelobe interference to maintain target visibility. This illustrates the Rydberg receiver's capability to distinguish closely spaced targets within operational limitations.

V. Discussions and Future Prospects

The Rydberg atomic receiver allows for the tuning of atomic energy levels through the adjustment of laser frequency, facilitating quasi-continuous frequency coverage from DC to THz, without replacing frequency-dependent RF sensing and mixing components. However, AC-Stark tuning is not a lossless translation of an isolated resonance. The tuning field modifies the Rydberg sublevel and dressed-state structure, redistributes the spectral response, and may reduce the effective transition dipole moment. These effects are experimentally manifested as reduced EIT/AT peak height, increased linewidth, or asymmetric AT peaks, which decrease the local response slope $|\partial S/\partial E_{\text{sig}}|$ and thereby increase the minimum detectable electric field. Similar sensitivity degradation under Stark- or dressing-based tuning has been reported in previous Rydberg electrometry studies [32], [33]. Therefore, the additional frequency tunability is obtained at the cost of possible sensitivity degradation, which remains a limitation of the present implementation. Frequency agility encounters fundamental constraints, as the transition between operational frequencies necessitates laser relocking and thermal restabilization. This significantly limits real-time target tracking and the response to dynamic scenes. The current latency significantly exceeds the microsecond-scale beam switching capabilities of electronic systems. In addition, this temporal latency introduces challenges for tracking moving targets, since the bandwidth is synthesized over the sweep duration.

For a target with signed radial velocity v_r, the echo can experience a Doppler shift $|f_D| \approx 2|v_r|f_c/c$. When $|f_D|$ becomes comparable to the atomic receiver's effective EIT-based sensing bandwidth B_{EIT}, the response may deviate from the flat-gain regime. In typical moderate-speed scenarios, however, $|f_D| \ll B_{\text{EIT}}$ and the gain variation is negligible. Consequently, the dominant motion artifact is an additional velocity-dependent phase term, $-\frac{4\pi f_k}{c}v_r t_k$. This error can be mitigated computationally by incorporating velocity estimation into the ranging model, or physically by reducing the sweep duration via rapid electro-optic laser retuning and fast state switching technologies. Emerging rapid-retuning laser technologies have the potential to meet the future demands of atomic radar systems for high-dynamic target tracking and high-throughput imaging [35].

The constraints of the darkroom size and laser performance restrict our ability to attain a higher equivalent bandwidth and increased frequency-domain sampling. Under the present eight-tone configuration, sparse and non-uniform frequency sampling produces a non-ideal range point-spread function with relatively high sidelobes and ambiguity peaks. Coherent environmental multipath and LO leakage, together with residual frequency-dependent atomic-response and phase-calibration errors, introduce additional spurious responses. Although CS-Rydberg substantially suppresses these artifacts, as supported by the ablation results in Fig. 6, it cannot completely eliminate them under the current laboratory conditions. Further suppression may be achieved through denser or optimized frequency placement, frequency-domain sidelobe weighting, complex-domain background and multipath calibration, and joint sparse reconstruction over multiple sweeps.

Accordingly, the tested range of 1.6–1.9 m should be interpreted as a constraint of the present laboratory prototype rather than as a fundamental sensing-range limit of the Rydberg atomic receiver. It is also important to distinguish range resolution from maximum detection range. The former is primarily determined by the synthesized frequency span, whereas the latter is governed by the radar link budget, including transmit power, antenna gains, and target radar cross section. To extend the detection range from the present laboratory scale to tens or hundreds of meters and beyond, the system must overcome the $1/R^2$ propagation loss of the echo field. The maximum achievable range is fundamentally governed by the radar link budget, requiring the received electric field $|E_{\mathrm{echo}}|$ to exceed the sensitivity threshold defined by $|E_{\mathrm{echo}}| \gtrsim \sigma_{\mathrm{NEF}}/\sqrt{\tau}$, where σ_{NEF} is the atomic sensitivity spectral density and τ is the coherent integration time. Consequently, long-range operation necessitates engineering optimizations such as high-sensitivity Rydberg atomic energy-level design, increasing transmit power, employing high-gain receiver antennas to focus the weak field onto the vapor cell, and extending the integration time τ to suppress noise. A mature conventional coherent receiver can readily perform the present short-range ranging task and currently offers clear advantages in instantaneous bandwidth, tuning speed, integration maturity, and operational robustness. Therefore, the present work does not claim superior short-range radar performance over conventional receivers. Its contribution is to demonstrate the feasibility of atomic RF-to-optical sensing and mixing while retaining coherent stepped-frequency ranging capability. The inherent quantum traceability and absolute calibration capabilities render the atomic receiver particularly suitable as a reference receiver in high-precision electromagnetic field metrology, such as RF antenna testing or radar cross-section measurements.

Several essential technologies require additional exploration to fully harness the potential of these applications. It is feasible to transition from zero-IF to heterodyne detection. A small frequency offset in the reference field is sufficient to convert the signal to an intermediate frequency, thereby mitigating baseband noise. This may also reduce phase errors associated with gain variations and low-frequency disturbances. A rigorous performance comparison with a conventional coherent receiver will additionally require both systems to be evaluated under matched transmit power, antennas, frequency grid, synthesized bandwidth. Such a controlled benchmark remains an important subject of future work.

VI. Conclusion

In this paper, we have introduced and experimentally demonstrated a transformative radar ranging methodology based on Rydberg atomic detection, addressing fundamental challenges faced by conventional radar front-ends. The atomic receiver architecture utilises quantum-optical interactions in caesium vapor cells to facilitate RF-to-optical signal conversion, eliminating the need for conventional RF components like mixers, amplifiers, and filters. Utilising a stepped-frequency method alongside laser frequency tuning and AC-Stark shift techniques, we have successfully synthesized a 1-GHz equivalent bandwidth via sparse stepped-frequency sampling across 2.6–3.6 GHz, facilitating centimeter-level precision in ranging. This study presents a nonlinear response model for a Rydberg atomic receiver. By implementing a nonlinear compensation scheme, we have achieved an extension of its linear dynamic range by more than 7 dB. We have developed a specialised CS-Rydberg signal-processing framework using compressive sensing. The experimental results indicate that the atomic radar attains a ranging accuracy of RMSE $= 1.06$ cm, with resolvable target separations observed to be down to 15 cm in controlled sparse scenarios.

The results indicate significant support for the practical viability and future potential of quantum sensing utilising Rydberg atomic receivers. This study offers essential experimental validation and theoretical foundations, facilitating significant progress in precision remote sensing and electromagnetic calibration within next-generation radar systems.

References

[1] C. L. Degen et al., "Quantum sensing," *Rev. Mod. Phys.*, vol. 89, no. 3, 2017, Art. no. 035002.

[2] S. Pirandola, B. R. Bardhan, T. Gehring, C. Weedbrook, and S. Lloyd, "Advances in photonic quantum sensing," *Nature Photon.*, vol. 12, no. 12, pp. 724–733, Dec. 2018.

[3] L. Maccone and C. Ren, "Quantum radar," *Phys. Rev. Lett.*, vol. 124, no. 20, 2020, Art. no. 200503.

[4] R. Assouly, R. Dassonneville, T. Peronnin, A. Bienfait, and B. Huard, "Quantum advantage in microwave quantum radar," *Nature Phys.*, vol. 19, no. 10, pp. 1418–1422, Oct. 2023.

[5] W. Wiesbeck and L. Sit, "Radar 2020: The future of radar systems," in *Proc. Int. Radar Conf.*, Oct. 2014, pp. 1–6.

[6] Z. Xiao, T. Mao, Z. Han, and X.-G. Xia, "Near space communications: A new regime in space-air-ground integrated networks," *IEEE Wireless Commun.*, vol. 29, no. 6, pp. 38–45, Dec. 2022.

[7] C. Hu et al., "Distributed spaceborne SAR: A review of systems, applications, and the road ahead," *IEEE Geosci. Remote Sens. Mag.*, vol. 13, no. 2, pp. 329–361, Jun. 2025.

[8] J. A. Sedlacek, A. Schwettmann, H. Kübler, R. Löw, T. Pfau, and J. P. Shaffer, "Microwave electrometry with Rydberg atoms in a vapour cell using bright atomic resonances," *Nature Phys.*, vol. 8, no. 11, pp. 819–824, Nov. 2012.

[9] M. Jing et al., "Atomic superheterodyne receiver based on microwave-dressed Rydberg spectroscopy," *Nature Phys.*, vol. 16, no. 9, pp. 911–915, Sep. 2020.

[10] S. Borówka, U. Pylypenko, M. Mazelanik, and M. Parniak, "Continuous wideband microwave-to-optical converter based on room-temperature Rydberg atoms," *Nature Photon.*, vol. 18, no. 1, pp. 32–38, Jan. 2024.

[11] S. Yuan, M. Jing, H. Zhang, L. Zhang, L. Xiao, and S. Jia, "Isotropic antenna based on Rydberg atoms," *Opt. Exp.*, vol. 32, no. 5, pp. 8379–8388, 2024.

[12] J. A. Sedlacek, A. Schwettmann, H. Kübler, and J. P. Shaffer, "Atom-based vector microwave electrometry using Rubidium Rydberg atoms in a vapor cell," *Phys. Rev. Lett.*, vol. 111, no. 6, Aug. 2013, Art. no. 063001.

[13] Y. Wang et al., "Precise measurement of microwave polarization using a Rydberg atom-based mixer," *Opt. Exp.*, vol. 31, no. 6, pp. 10449–10457, 2023.
[14] S. Bao et al., "Polarization spectra of Zeeman sublevels in Rydberg electromagnetically induced transparency," *Phys. Rev. A, Gen. Phys.*, vol. 94, no. 4, Oct. 2016, Art. no. 043822.
[15] M. T. Simons, A. H. Haddab, J. A. Gordon, and C. L. Holloway, "A Rydberg atom-based mixer: Measuring the phase of a radio frequency wave," *Appl. Phys. Lett.*, vol. 114, no. 11, pp. 114101-1–114101-4, 2019.
[16] S. Berweger et al., "Closed-loop quantum interferometry for phase-resolved Rydberg-atom field sensing," *Phys. Rev. Appl.*, vol. 20, no. 5, Nov. 2023, Art. no. 054009.
[17] A. Kale, R. Thirumuru, and V. S. R. Pasupureddi, "Wideband channelized sub-sampling transceiver for digital RF memory based electronic attack system," *Aerosp. Sci. Technol.*, vol. 51, pp. 34–41, Apr. 2016.
[18] R.-H. Xing et al., "Chip-scale Rydberg atomic electrometer," *Chip*, vol. 5, no. 3, Sep. 2026, Art. no. 100187.
[19] F. Zhang et al., "Quantum wireless sensing: Principle, design and implementation," in *Proc. 29th Annu. Int. Conf. Mobile Comput. Netw.*, Oct. 2023, pp. 1–15.
[20] A. K. Robinson, N. Prajapati, D. Senic, M. T. Simons, and C. L. Holloway, "Determining the angle-of-arrival of a radio-frequency source with a Rydberg atom-based sensor," *Appl. Phys. Lett.*, vol. 118, no. 11, pp. 114001-1–114001-4, 2021.
[21] Y. Yan, J. Yuan, L. Zhang, L. Xiao, S. Jia, and L. Wang, "Three-dimensional location system based on an L-shaped array of Rydberg atomic receivers," *Opt. Lett.*, vol. 48, no. 15, pp. 3945–3948, 2023.
[22] R. Mao, Y. Lin, Y. Fu, Y. Ma, and K. Yang, "Digital beam-forming and receiving array research based on Rydberg field probes," *IEEE Trans. Antennas Propag.*, vol. 72, no. 2, pp. 2025–2029, Feb. 2024.
[23] G. Gao et al., "Rydberg communication antennas with self-decoupling for dynamic radar interference based on heterodyne technology," *Appl. Phys. Lett.*, vol. 126, no. 13, pp. 134002-1–134002-7, Mar. 2025.
[24] S. M. Bohaichuk, D. Booth, K. Nickerson, H. Tai, and J. P. Shaffer, "Origins of Rydberg-atom electrometer transient response and its impact on radio-frequency pulse sensing," *Phys. Rev. Appl.*, vol. 18, no. 3, Sep. 2022, Art. no. 034030.
[25] D. H. Meyer, J. C. Hill, P. D. Kunz, and K. C. Cox, "Simultaneous multiband demodulation using a Rydberg atomic sensor," *Phys. Rev. Appl.*, vol. 19, no. 1, Jan. 2023, Art. no. 014025.
[26] M. Arik and O. B. Akan, "Collaborative mobile target imaging in UWB wireless radar sensor networks," *IEEE J. Sel. Areas Commun.*, vol. 28, no. 6, pp. 950–961, Aug. 2010.
[27] N. Prajapati et al., "TV and video game streaming with a quantum receiver: A study on a Rydberg atom-based receiver's bandwidth and reception clarity," *AVS Quantum Sci.*, vol. 4, no. 3, pp. 035001-1–035001-8, 2022.
[28] R. E. Sapiro, G. Raithel, and D. A. Anderson, "Time dependence of Rydberg EIT in pulsed optical and RF fields," *J. Phys. B, At., Mol. Opt. Phys.*, vol. 53, no. 9, May 2020, Art. no. 094003.
[29] M. Cui, Q. Zeng, Z. Wang, and K. Huang, "Realizing quantum wireless sensing without extra reference sources: Architecture, algorithm, and sensitivity maximization," *IEEE Trans. Signal Process.*, vol. 74, pp. 1570–1585, 2026.
[30] Y. Tang, H. Zhou, C. Yang, S. Ren, S. Wang, and C. Lu, "Noise performance of a Rydberg atomic receiver," *Phys. Rev. A, Gen. Phys.*, vol. 112, no. 4, Oct. 2025, Art. no. 043106.
[31] N. Šibalić, J. D. Pritchard, C. S. Adams, and K. J. Weatherill, "ARC: An open-source library for calculating properties of alkali Rydberg atoms," *Comput. Phys. Commun.*, vol. 220, pp. 319–331, Nov. 2017.
[32] Y. Shi et al., "Tunable frequency of a microwave mixed receiver based on Rydberg atoms under the Zeeman effect," *Opt. Exp.*, vol. 31, no. 22, pp. 36255–36262, 2023.
[33] K. Ouyang, Y. Shi, M. Lei, and M. Shi, "Continuous broad-band microwave electric field measurement in Rydberg atoms based on the DC stark effect," *Appl. Phys. Lett.*, vol. 123, no. 26, pp. 264001-1–264001-5, 2023.
[34] K. Yang, R. Mao, Q. An, J. Li, Z. Sun, and Y. Fu, "Amplitude-modulated RF field Rydberg atomic sensor based on homodyne technique," *Sens. Actuators A, Phys.*, vol. 351, Mar. 2023, Art. no. 114167.
[35] B. Stern et al., "Broadly and finely tunable hybrid silicon laser with nanosecond-scale switching speed," *Opt. Lett.*, vol. 45, no. 22, pp. 6198–6201, 2020.

Minze Chen received the B.S. degree from Beijing Institute of Technology, Beijing, China, in 2018, and the M.S. degree from Tsinghua University, Beijing, in 2022, where he is currently pursuing the Ph.D. degree with the School of Interdisciplinary Science. He was selected for the special talent cultivation project for Ph.D. students of China Association for Science and Technology. His research interests include quantum sensing, atomic sensors, and Rydberg physics.

Tianqi Mao (Member, IEEE) received the B.S., M.S. (Hons.), and Ph.D. (Hons.) degrees from Tsinghua University, Beijing, China, in 2015, 2018, and January 2022, respectively. He is currently an Associate Professor with the School of Interdisciplinary Science, Beijing Institute of Technology, Beijing. He has authored over 70 journals and conference papers. His research interests include modulation, waveform design, integrated sensing and communication, and Rydberg atomic communication and sensing. He was the Workshop Co-Chair of IEEE ICC 2026, IEEE GLOBECOM 2026, IEEE WCNC 2026, IEEE PIMRC 2026, and IEEE PIMRC 2025, regarding next-evolution waveform and modulation; and the Organizer of an industry panel at IEEE WCNC 2024. He is currently an Associate Editor of IEEE TRANSACTIONS ON COMMUNICATIONS, IEEE TRANSACTIONS ON VEHICULAR TECHNOLOGY, and IEEE COMMUNICATIONS LETTERS. He was a Lead Guest Editor of IEEE WIRELESS COMMUNICATIONS and *IEEE Network*; a Guest Editor of IEEE TRANSACTIONS ON MOLECULAR, BIOLOGICAL, AND MULTI-SCALE COMMUNICATIONS and the IEEE OPEN JOURNAL OF THE COMMUNICATIONS SOCIETY; and an Associate Editor of the IEEE OPEN JOURNAL OF VEHICULAR TECHNOLOGY.

Zhiao Zhu received the B.S. degree from Zhengzhou University, Zhengzhou, China, in 2023. He is currently pursuing the Ph.D. degree in information and communication engineering with Beijing Institute of Technology, Beijing, China. He began his graduate studies as a master's student in 2023 and transferred to the doctoral program in 2025. His research interests include quantum sensing, atomic sensors, Rydberg physics, and integrated Rydberg three-photon systems.

Haonan Feng received the B.S. degree from Hunan University, Changsha, China, in 2019, and the M.S. degree from Beihang University, Beijing, China, in 2022. He is currently pursuing the Ph.D. degree with the School of Interdisciplinary Science, Beijing Institute of Technology, Beijing. He worked as an Engineer with the Yangtze Delta Region Academy of Beijing Institute of Technology (Jiaxing), Jiaxing, China, for one year. His research interests include Rydberg physics, quantum sensors, microwave engineering, and the integration of metasurface materials with Rydberg atom sensors.

Ge Gao received the B.E. and M.Eng. degrees from Beihang University, Beijing, China, in 2021 and 2024, respectively. She is currently pursuing the Ph.D. degree with the School of Information and Electronics, Beijing Institute of Technology, Beijing. Her research focuses on Rydberg atoms for microwave electric-field sensing.

Zhonghuai Wu received the Ph.D. degree from The University of New South Wales, Sydney, Australia. He is currently a Professor with the School of Interdisciplinary Science, Beijing Institute of Technology, Beijing, China.

Wei Xiao received the Ph.D. degree from Peking University, Beijing, China, in 2022. He is currently an Assistant Professor with the School of Interdisciplinary Science, Beijing Institute of Technology, Beijing. His research focuses on atomic, molecular, and optical (AMO) physics, with an emphasis on quantum precision measurement of electromagnetic fields and its practical applications.

Zhongxiang Li received the B.E. degree from Beijing Institute of Technology, Beijing, China, in 2011, the M.E. degree from North China University of Technology, Beijing, in 2014, and the Ph.D. degree from Beihang University, Beijing, in 2022. From 2022 to 2025, he was a Post-Doctoral Researcher with Beijing Institute of Technology, where he has been with the School of Interdisciplinary Science and the Yangtze Delta Region Academy since 2025. His research interests include extreme-environment sensing, advanced optical detection, and intelligent signal processing.

Dezhi Zheng was born in Liaoning, China, in 1978. He received the B.S. degree in mechanical engineering and the Ph.D. degree in precision instruments and mechanical engineering from Beihang University, Beijing, China, in 2000 and 2006, respectively. Since 2006, he has been a Professor at Beihang University and Beijing Institute of Technology. From 2014 to 2015, he was a Visiting Scholar with the University of Victoria, Victoria, BC, Canada. He is also the Secretary of the School Party Committee, School of Interdisciplinary Science, Beijing Institute of Technology. He is the author of more than 50 articles and more than ten inventions. His research interests include sensor technology, signal detection, and signal processing.

George K. Karagiannidis (Fellow, IEEE) received the Ph.D. degree in telecommunications engineering from the Electrical Engineering Department, University of Patras, Greece, in 1998. He is currently a Professor with the Electrical and Computer Engineering Department, Aristotle University of Thessaloniki, Thessaloniki, Greece; and the Head of Wireless Communications and Information Processing (WCIP) Group. His research interests are in the areas of wireless communications systems and networks, signal processing, optical wireless communications, wireless power transfer, and signal processing for biomedical engineering. He recently received three prestigious awards: the 2021 IEEE ComSoc RCC Technical Recognition Award, the 2018 IEEE ComSoc SPCE Technical Recognition Award, and the 2022 Humboldt Research Award from the Alexander von Humboldt Foundation. He is one of the Highly Cited Authors across all areas of electrical engineering, recognized by Clarivate Analytics as a Web of Science Highly Cited Researcher for ten consecutive years (2015–2024). He is also the Editor-in-Chief of IEEE TRANSACTIONS ON COMMUNICATIONS. Previously, he was the Editor-in-Chief of IEEE COMMUNICATIONS LETTERS.

Zhaocheng Wang (Fellow, IEEE) received the B.S., M.S., and Ph.D. degrees from Tsinghua University in 1991, 1993, and 1996, respectively.

Since 2009, he has been a Professor with the Department of Electronic Engineering, Tsinghua University, where he is currently the Director of the Broadband Communication Key Laboratory, Beijing National Research Center for Information Science and Technology (BNRist). He has authored or co-authored two books, which have been selected by the IEEE Press Series on Digital and Mobile Communication (Wiley–IEEE Press). He has also authored or co-authored more than 160 peer-reviewed journal articles. He holds 72 U.S./EU granted patents, 23 of them as the first inventor. His research interests include wireless communications, millimeter-wave communications, and optical wireless communications. He is a fellow of the Institution of Engineering and Technology. He was a recipient of the ICC 2013 Best Paper Award, the OECC 2015 Best Student Paper Award, the 2016 IEEE Scott Helt Memorial Award, the 2016 IET Premium Award, the 2016 National Award for Science and Technology Progress (First Prize), the ICC 2017 Best Paper Award, the 2018 IEEE ComSoc Asia–Pacific Outstanding Paper Award, and the 2020 IEEE ComSoc Leonard G. Abraham Prize.

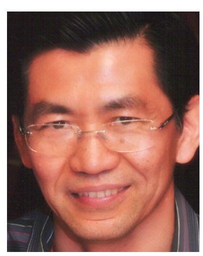

Sheng Chen (Life Fellow, IEEE) received the B.Eng. degree in control engineering from East China Petroleum Institute, Dongying, China, in January 1982, the Ph.D. degree in control engineering from the City St George's University of London, London, U.K., in September 1986, and the D.Sc. degree from the University of Southampton in August 2005.

He is currently an Emeritus Professor with the University of Southampton, Southampton, U.K. From 1986 to 1999, he held research and academic appointments with The University of Sheffield, The University of Edinburgh, and the University of Portsmouth, U.K. In September 1999, he joined the School of Electronics and Computer Science, University of Southampton, and retired in June 2026. Since then, he has been an University Visitor with the School of Electronics and Computer Science, University of Southampton. In 2023, he was appointed a Distinguished Professor at the Ocean University of China, Qingdao, China. He has established an academic career of over 40 years in adaptive signal processing, wireless communications, neural networks, and machine learning. He has authored or co-authored over 750 research papers. He has over 23 000 Web of Science citations with an H-index of 67 and over 44 000 Google Scholar citations with an H-index of 88.

Prof. Chen was elected a fellow of the Royal Academy of Engineering in 2014. He is also a fellow of the Asia–Pacific Artificial Intelligence Association, the Industry Academy of the International Artificial Intelligence Industry Alliance, and the Institution of Engineering and Technology. He was one of the original 200 ISI Highly Cited Researchers in engineering in March 2004. He received the IEEE Communications Society Signal Processing and Computing for Communications Technical Recognition Award in 2025.